Characterizing the nuclear models informed by PREX and CREX: A view from Bayesian inference

Tianqi Zhao [1,2,3,*] Zidu Lin [4,†] Bharat Kumar [5,‡] Andrew W. Steiner [4,6,§] and Madappa Prakash [3,‖]

[1]Department of Physics, University of California Berkeley, Berkeley, California 94720, USA
[2]Institute for Nuclear Theory, University of Washington, Seattle, Washington 98195, USA
[3]Department of Physics and Astronomy, Ohio University, Athens, Ohio 45701, USA
[4]University of Tennessee, Knoxville, Tennessee 37996, USA
[5]Department of Physics & Astronomy, National Institute of Technology, Rourkela 769008, India
[6]Physics Division, Oak Ridge National Laboratory, Oak Ridge, Tennessee 37830, USA

(Received 14 June 2024; revised 2 May 2025; accepted 13 November 2025; published 26 December 2025)

Measurements from the weak charge radius experiments on ^{48}Ca (CREX) and ^{208}Pb (PREX) challenge existing nuclear models. In the post-PREX-CREX era, it is unclear if current models can simultaneously describe weak charge distributions along with accurate measurements of binding energy and charge radii. In this work, we explore the parameter space of relativistic and nonrelativistic models to study the differences between the electric and weak form factors, $\Delta F = F_{\rm ch} - F_W$, in ^{48}Ca and ^{208}Pb. We show, for the first time, which aspects of mean-field models are the most important in determining the relative magnitude of the neutron skin in lead and calcium nuclei. We carefully disentangle the tension between the PREX-2/CREX constraints and the ability of the relativistic mean field and Skyrme models to accurately describe binding energies and charge radii. We find that the nuclear symmetry energy coefficient $S_{\rm V}$ and the isovector spin-orbit coefficient b'_4 play different roles in determining ΔF of ^{48}Ca and ^{208}Pb. Consequently, adjusting $S_{\rm V}$ or b'_4 shifts predicted ΔF values toward or away from PREX-2/CREX measurements. Additionally, $S_{\rm V}$ and the slope L are marginally correlated given the prior constraints of our Bayesian inference, allowing us to infer them separately from PREX-2/CREX data.

DOI: 10.1103/472x-9cxj

I. INTRODUCTION

One of the goals in nuclear physics is the construction of a unified theory that describes the basic properties of nuclei and neutron star (NS) observables. Historically, nuclear Hamiltonians have been constrained by binding energies, charge radii, and the energies of giant resonances. The requirement of simultaneously describing the charge distributions of a variety of isotopes has spurred the improvement of nuclear structure theories, including those based on *ab initio* calculations, Skyrme effective interactions, and relativistic mean-field (RMF) calculations [1–5]. The Skyrme force is an effective interaction used in nuclear Hartree-Fock approximations, characterized by a zero-range interaction with density-dependent terms. On the other hand, the RMF theory is a relativistic framework describing interacting nucleonic Dirac fields and mesonic mean fields. In RMF theory, the basic fields typically included are the scalar (σ), vector (ω), and vector-isovector fields. The RMF can be directly related to Skyrme models by considering a nonrelativistic expansion [6], which will be discussed in more details in this work. Neutron distributions in finite nuclei are less sensitive to binding energies and charge radii [7], leading to less-constrained isovector interactions in traditional nuclear models. Nonetheless, isospin-dependent interactions play a crucial role in describing NS properties. Recently, information about differences between the electric and weak form factors (calculated as in Appendix C) $\Delta F = F_{\rm ch} - F_W$ of two neutron-rich magic nuclei, ^{208}Pb and ^{48}Ca, has been model-independently measured via parity-violating electron scattering experiments [8,9] and many theoretical models [10–16] have been proposed to interpret the measurements from PREX-2 and CREX. However, it is important to note that these models generally succeed in describing either PREX-2 or CREX measurements, but face difficulties in simultaneously explaining both sets of data.

Can existing forms of relativistic RMF models and nonrelativistic Skyrme models simultaneously describe the weak charge distributions inferred by PREX-2/CREX, while maintaining consistency with the basic ground-state properties of finite nuclei? If so, what would be the implications for the isospin-dependent interactions of such models? In this work, we investigate this issue by extensively surveying the parameter space of both RMF and Skyrme models to study their dependence on $S_{\rm V}$, L, and isovector spin-orbit

*Contact author: tianqi.zhao@berkeley.edu
†Contact author: zlin23@utk.edu
‡Contact author: kumarbh@nitrkl.ac.in
§Contact author: awsteiner@utk.edu
‖Contact author: prakash@ohio.edu

Published by the American Physical Society under the terms of the Creative Commons Attribution 4.0 International license. Further distribution of this work must maintain attribution to the author(s) and the published article's title, journal citation, and DOI.

interactions. Using Bayesian inference, we analyze the information provided by PREX-2 and CREX measurements, detailed further in the Appendixes and data repository [17]. Our approach also incorporates the fundamental ground-state properties of ^{48}Ca, ^{90}Zr, and ^{208}Pb, in line with previous studies [12,18,19]. Notably, we focus on the physical properties of the Skyrme and RMF models that are consistent with PREX-2/CREX experiments and quantify the extent to which these models can jointly reconcile PREX-2/CREX data with other existing nuclear measurements.

II. S_V-L INFERRED BY JOINT PREX-2/CREX MEASUREMENTS

For densities of relevance to nuclei, the energy of asymmetric nuclear matter can be expressed as the sum of symmetric nuclear matter (SNM) and symmetry energies as

$$E(n_p, n_n) = E(n_p = n_n = n/2) + S(n_p, n_n), \tag{1}$$

where n_n and n_p are the neutron and proton densities, respectively, and n is their sum. The SNM energy E can be expanded around the saturation density n_0, at which the SNM energy reaches its minimum:

$$E(n_p = n_n = n/2) = -B + \frac{K_0}{18n_0^2}(n - n_0)^2 + \cdots. \tag{2}$$

Here, B is the binding energy and K_0 is the SNM incompressibility. To good approximation, the symmetry energy S is given by the quadratic term in the expansion (asymmetry) parameter $(n_n - n_p)/n$:

$$S(n_p, n_n) = S(n)\left(\frac{n_n - n_p}{n}\right)^2 + \cdots, \tag{3}$$

where $S(n)$ is the density-dependent symmetry energy. An alternative definition based on pure neutron matter (PNM), $S(n) = S(n_n = n, n_p = 0)$, has also been used [20]. The deviation of $S(n)$ between these two definitions represents the breaking of the quadratic approximation, which is usually small for most Skyrme models [21–24]. However, such a deviation can be larger in some other models [25]. In RMF models, the inclusion of the δ meson with large Yukawa coupling breaks the quadratic approximation significantly as shown in Ref. [26] and Table II in the Appendixes. Ignoring corrections that are quartic in the isospin asymmetry, $S(n)$ can be expanded around the saturation density as

$$S(n) = S_V + \frac{L}{3n_0}(n - n_0) + \frac{K_{sym}}{18n_0^2}(n - n_0)^2 + \cdots, \tag{4}$$

where S_V is the bulk symmetry energy, L refers to the slope of the symmetry energy slope, and K_{sym} refers to the curvature of the symmetry energy.

Neutron skin thicknesses of neutron-rich nuclei are primarily determined by $S(n)$ [27]. The strong correlation between L and the neutron skin thickness has been extensively studied using Skyrme and RMF models of nuclei [11,28]. The neutron skin can also be understood using a simple droplet model in terms of the competition between the bulk symmetry term $S_V I$ and the surface term $\Delta R_{np} Q$ [29–31]. Here, $I = (N - Z)/A$, with N and Z being the neutron and proton numbers in a nucleus and A their sum, ΔR_{np} is the neutron-proton radius difference, and Q is the surface stiffness parameter. The first of these competing terms is closely related to the properties of bulk matter in the central regions of nuclei and the second relates also to the spin-orbit interaction. In Fig. 1, we present the S_V and L constrained by ΔF^{Ca48} and ΔF^{Pb208}, without assuming the correlation between them. Given ΔF^{Ca48}, ΔF^{Pb208}, S_V, and L sampled from our Bayesian posterior, we find that S_V and L can be well approximated by a linear combination of ΔF^{Ca48} and ΔF^{Pb208} as

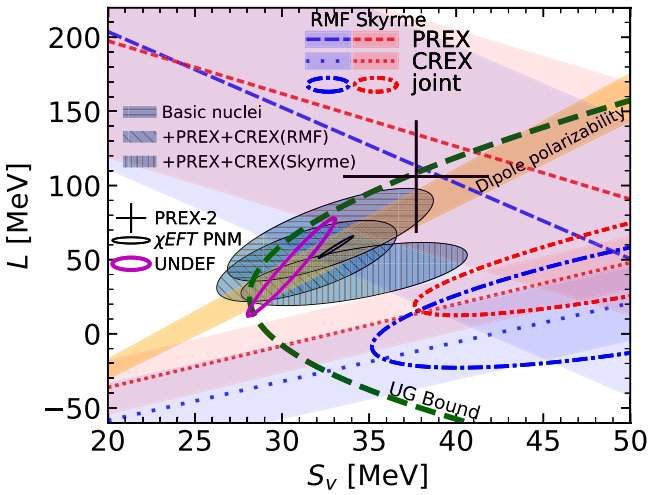


FIG. 1. Symmetry energy parameters S_V and L constrained by parity-violating asymmetry of ^{48}Ca (CREX) and ^{208}Pb (PREX-2). The dashed (dotted) line and the corresponding band represent the mean and 1σ band of PREX-2 (CREX) alone based on the correlations in Eqs. (5) and (6). Dash-dotted ellipse represents the 1σ contour of joint PREX-2/CREX constraints. The PREX-2 analysis [11] as well as constraints from the unitary gas conjecture [32] and dipole polarizability [33] are shown for comparison. The horizontally shaded ellipse shows the 1σ contour of the posterior with basic nuclei constraints, corresponding to the yellow distribution shown in Fig. 2, whereas the other two shaded ellipses show the posterior with +PREX + CREX for Skyrme (vertical shade) and RMF (diagonal shade) models. The magenta ellipse shows the UNEDF correlation considering properties of more nuclei. The small black ellipse shows the correlation from chiral effective field theory (EFT) calculation of PNM [35].

$$S_V = a\Delta F^{Ca48} + b\Delta F^{Pb208} + c, \tag{5}$$

$$L = a'\Delta F^{Ca48} + b'\Delta F^{Pb208} + c'. \tag{6}$$

The slope coefficients a, b, a', and b', as well as the intercept parameters c and c', are determined by fitting them to the posterior distribution of $(\Delta F^{Ca48}, \Delta F^{Pb208}, S_V)$ and $(\Delta F^{Ca48}, \Delta F^{Pb208}, L)$, respectively. These parameters may reflect the inherent structure of RMF and Skyrme models and could be insensitive to the Bayesian constraints. All the sampled points from the posterior are presented in the Appendix D. The fitted slope and intercept parameters are summarized in Table I. The precision of the fitting formula in Eq. (5) remains within 10% (1σ) for both Skyrme and RMF models. Given the mean and standard deviation of ΔF^{Pb208} and ΔF^{Ca48} measured by PREX-2/CREX and the

TABLE I. Parameters for the fitting formulas of S_V [Eq. (5)] and L [Eq. (6)] are in units of MeV, and for b'_4 [Eq. (12)], they are in units of fm^4.

	a	b	c	a'	b'	c'	a''	b''	c''
RMF	-575.2 ± 5.1	916.3 ± 4.6	32.2 ± 3.7	2938.7 ± 43.5	2420.6 ± 33.9	-149.8 ± 25.6	-31.8 ± 0.2	23.5 ± 0.1	0.94 ± 0.11
Skyrme	-503.2 ± 7.8	945.2 ± 5.5	31.9 ± 2.9	1791.2 ± 27.2	2652.0 ± 19.0	-91.5 ± 10.1	-52.0 ± 0.4	27.8 ± 0.3	1.67 ± 0.15

linear relationship in Eqs. (5) and (6), we obtain the mean and covariance of S_V and L to be

$$(\bar{S}_V, \bar{L}) = (56.7,\ 66.8)_{\text{Skyrme}},\ (53.8,\ 30.9)_{\text{RMF}},$$
$$\sqrt{\text{cov}} = \begin{pmatrix} 19.6 & 31.2 \\ 31.2 & 56.5 \end{pmatrix}_{\text{Skyrme}},\ \begin{pmatrix} 19.5 & 31.0 \\ 31.0 & 66.3 \end{pmatrix}_{\text{RMF}}, \quad (7)$$

in units of MeV for Skyrme and RMF models, respectively. See the red and blue dash-dotted ellipses in Fig. 1. The covariance is dominated by the experimental error of ΔF^{Ca48} or ΔF^{Pb208}. The precision of the fitting formulas in Eqs. (5) and (6) serves as a minor modification.

Comparing to previous PREX-2 analysis [11], our constraints on S_V and L are less affected by the basic finite nuclei ground-state properties. The overlapping region of these two bands represents the range of S_V, L inferred by the 1σ experimental measurements from PREX-2/CREX, which is quantitatively described by Eq. (7). In Fig. 2, we analyze the evolution of the posterior distributions for S_V and L under five different constraint sets: basic nuclear constraints as the "minimum setting," corresponding to horizontally shaded ellipse in Fig. 1; inclusion of either PREX-2 or CREX experimental data; inclusion of both PREX-2/CREX experimental data, corresponding to vertically and diagonally shaded ellipse in Fig. 1; and inclusion of additional dipole polarizability constraint. In the upper two panels for the Skyrme model, we observe that the range of S_V is approximately [20, 50] MeV,

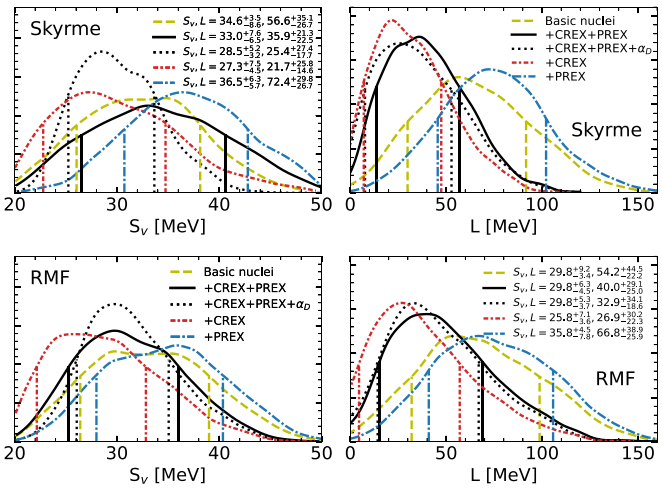


FIG. 2. The posterior distribution of bulk symmetry energy S_V and symmetry energy slope L at saturation density constrained by basic nuclei constraints (dashed yellow), +PREX experiment (dash-dotted blue), +CREX experiment (dash-dotted red), and +PREX + CREX experiment (solid black). The dotted black curve includes additional constraint from dipole polarizability [33]. The vertical lines correspond to 1σ asymmetric uncertainty. Details of prior and likelihood are discussed in the Appendixes.

whereas the range of L spans as [0, 150] MeV. In the upper right (Skyrme) and lower right (RMF) panels, the posteriors of L exhibit similar trends. The posteriors of L constrained by CREX (PREX-2) measurements have a mean smaller (larger) than that constrained by only basic properties of finite nuclei. Moreover, the posteriors of L constrained by both PREX-2 and CREX measurements have a mean lower than that without any neutron skin constraints, but slightly higher than the one that includes only the CREX constraint. This trend exists in both RMF and Skyrme models and aligns with previous studies using Skyrme [5,18,36] and RMF models [11,19,37]. The confidence level integral suggests a probability of inconsistency of 93% (1.8σ) for Skyrme models and 76% (1.2σ) for RMF models, significantly lower than other analyses showing over 2σ inconsistency [18,19,37]. Further details of our Bayesian inference and Monte Carlo sampling are provided in the Appendixes.

III. IMPACT OF SPIN-ORBIT INTERACTIONS

Unlike the Hamiltonian of infinite nuclear matter, the Hamiltonian of finite nuclei incorporates terms proportional to the derivative of isoscalar (isovector) densities, primarily arising from spin-orbit interactions. The impact of spin-orbit interactions on single-particle spectra and the charge distributions of various neutron-rich isotopes has been acknowledged and discussed in prior studies [38,39]. However, the isospin-dependent spin-orbit interactions are not well constrained, in comparison with other interactions constrained by isobaric analog states [40] and mirror nuclei [41]. Since the weak charge form factor F_W and the charge form factor F_{ch} for ^{208}Pb and ^{48}Ca are very close in value, the resulting difference $\Delta F = F_W - F_{\text{ch}}$ is relatively small—roughly, one order of magnitude smaller than F_W and F_{ch}. As a result, the influence of spin-orbit interactions becomes crucial in accurately determining the distribution of $\{\Delta F_{^{48}\text{Ca}}, \Delta F_{^{208}\text{Pb}}\}$ in our study. For the first time (as far as we are aware), we investigate the influence of spin-orbit interactions on both ΔF^{Ca48} and ΔF^{Pb208} across a very large parameter space encompassing both RMF and Skyrme parametrizations. This investigation is based on the posterior distribution incorporating constraints from PREX-2/CREX measurements. The spin-orbit interactions in Skyrme models are written as

$$H_{\text{SO}} = b_4 \mathbf{J} \cdot \nabla n + b'_4 (\mathbf{J}_n \cdot \nabla n_n + \mathbf{J}_p \cdot \nabla n_p), \quad (8)$$

where b_4 and b'_4 coefficients correspond to the isoscalar and isovector contributions of the spin-orbit potentials, respectively. To compare spin-orbit interactions in both relativistic and nonrelativistic models in a parallel manner, we recast the Dirac equation in Schrödinger form using the Foldy-Wouthuysen transformation, and the RMF spin-orbit

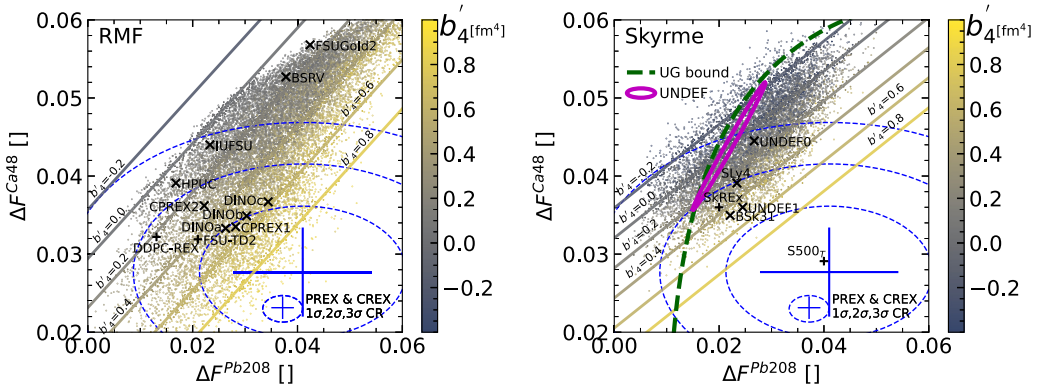


FIG. 3. Charge and weak form factor difference of ^{48}Ca and ^{208}Pb for samples of RMF (left) and Skyrme (right) model colored by the isovector spin-orbit parameter b'_4 in unit fm^4. Colorful lines correspond to the minimum χ^2 fitting of linear function same as Eqs. (5) and (6) with $b'_4 = [-0.2, 0, 0.2, 0.4, 0.6, 0.8]$. Constraints from unitary gas conjecture [32] and nuclei properties [34] are calculated from corresponding curves in Fig. 1 based on the correlation Eqs. (5) and (6). Blue dashed line shows 1-, 2-, and 3σ confidence regions of joint PREX-2/CREX results. "x" markers on the left panels are RMF models listed in the Appendix E. Reference and b'_4 for Skyrme models with marker "x" are discussed in the text. "+" markers represent the recently calibrated Skyrme model [18,42], the relativistic Hartree-Bogoliubov model [37], and RMF model with tensor interaction [26], which take different form of interactions. For readability, only part of RMF and Skyrme models are shown. A more comprehensive analysis of the b'_4 distribution of existing models is presented in the Appendix E.

contribution models can be approximated as

$$V_{\rm SO}^{p/n} = -\frac{2b_4}{r}\frac{d\rho_B}{dr} - \frac{b'_4}{r}\frac{d}{dr}[\rho_B \pm (\rho_p - \rho_n)], \tag{9}$$

with

$$b_4 \approx \frac{1}{4m^2}\left(\frac{g_\sigma^2}{m_\sigma^2} + \frac{g_\omega^2}{m_\omega^2} - \frac{g_\delta^2}{4m_\delta^2} - \frac{g_\rho^2}{4m_\rho^2}\right), \tag{10}$$

$$b'_4 \approx \frac{1}{8m^2}\left(\frac{g_\delta^2}{m_\delta^2} + \frac{g_\rho^2}{m_\rho^2}\right). \tag{11}$$

The detailed derivation of spin-orbit contributions in RMF models is provided in the Appendix B.

In Fig. 3, we present the distributions of $\{\Delta F^{\rm Ca48}, \Delta F^{\rm Pb208}\}$ colored by b'_4 in RMF and Skyrme models. As b'_4 increases, $\Delta F^{\rm Pb208}$ rises while $\Delta F^{\rm Ca48}$ drops, moving predictions closer to the PREX-2/CREX mean. Neutron skin thickness $\Delta R_{\rm np}$ follows the same trend. The detailed proton and neutron density profiles are presented in the Appendix F. We can fit the parameter b'_4 as

$$b'_4 = a''\Delta F^{\rm Ca48} + b''\Delta F^{\rm Pb208} + c'', \tag{12}$$

with the fit parameters in Table I. The fit yields $c'' = 1.69 \pm 0.15$ (Skyrme) and 0.93 ± 0.11 (RMF), which is well within PREX-2/CREX errors. This correlation with ΔF in PREX-2/CREX gives $b'_4 = 1.37 \pm 0.49$ fm^4 in Skyrme model, corresponding to a 90% lower bound of $b'_4 > 0.744$ fm^4. The widely used SLy4 model has $b_4 = b'_4 = 0.312$ fm^4 [43], which lies on the 2σ contour of the PREX-2/CREX measurement. Many successful Skyrme models [38,44–48] with $b_4 \neq b'_4$ have been developed, generally showing that larger b'_4 values correlate with better agreement with PREX-2/CREX. Most recently, an extended Skyrme model S500$_T$ [42] with $b'_4 = 1.27$—about three times that of BSk31 [48] and UNEDF1 [47]—was proposed to match the center of the PREX-2/CREX constraint, in agreement with the prediction of Eq. (12). For RMF models, Eq. (12) gives $b'_4 = 1.02 \pm 0.37$, corresponding to a 90% lower bound of $b'_4 > 0.544$ fm^4 or $g_\delta^2 + 1.65g_\rho^2 > 2433$ with Eq. (B17). Common RMF models without δ mesons (e.g., FSUGold2 [49] and IUFSU [50]) yield $b'_4 < 0.1$, outside the 2σ region; see, e.g., recent calibrated HPUA–C [51]. Even recent models like BSRV with weak isovector couplings remain insufficient [52]. However, models like DINOa–c, with large isovector Yukawa couplings ($g_\delta^2 > 1100$ and $g_\rho^2 > 800$), all surpass the 90% lower bound of $b'_4 > 0.544$ [10], and lie near the 1σ PREX-2/CREX region as in Fig. 3. Exploring the parameter space with large g_δ and g_ρ, we identify a parameter set, CPREX1 ($b'_4 = 0.652$), which resides on the 1σ upper (lower) edge of $\Delta F^{\rm Ca48}$ ($\Delta F^{\rm Pb208}$), and well within the 1σ joint contour. CPREX1 also yields reasonable nuclear properties for ^{48}Ca, ^{90}Zr, and ^{208}Pb, along with decent NS properties, featuring a maximum mass of $M_{\rm max} = 2.04$ M$_\odot$ and dimensionless tidal deformability of $\Lambda_{1.4} = 584$ within the GW170817 constraint [53]. Additionally, we introduce CPREX2 with an intermediate $b'_4 = 0.386$, closely aligned with Skyrme models like UNEDF1 and SV. Model parameters and other properties of CPREX are tabulated in the Appendix A. Their corresponding NS equation of states (EOSs) with crust calculated from the droplet model are available from the public GitHub repository [17].

IV. CONCLUSION AND DISCUSSION

In this work, we systematically investigated the influence of $S_{\rm V}$, L, and b'_4 on the ΔF of ^{48}Ca and ^{208}Pb based on Bayesian inference.

We identified a quasilinear relationship between the symmetry energy parameters ($S_{\rm V}$ and L) and the ΔF. This relationship exhibits a weak dependency on nuclear models. Unlike L, which is positively related to the ΔF values of both the ^{208}Pb and ^{48}Ca, $S_{\rm V}$ impacts ^{208}Pb and ^{48}Ca differently. This suggests that $S_{\rm V} \gtrsim 40$ MeV is favored by PREX-2/CREX measurements. The large $S_{\rm V}$ compared with empirical value (around 32 MeV) suggests the tension between the current nuclear models and joint PREX-2/CREX experiments.

TABLE II. σ meson mass and seven coupling constants of RMF models.

	m_σ (MeV)	g_σ^2	g_δ^2	g_ω^2	g_ρ^2	κ (MeV)	λ	$\Lambda_{\omega\rho}$	ζ
CPREX1	452.852	60.4489	1348.64	96.8552	948.802	12.1881	−0.034 2058	0.002 275 75	0.005 872 31
CPREX2	484.272	77.601	754.613	120.463	589.842	7.6226	−0.021 1199	0.003 350 68	0.011 6056

Additionally, we found that the isovector parts of the spin-orbit interactions in both Skyrme and RMF models influence the neutron skin of ^{208}Pb and ^{48}Ca *differently*. Recently, the authors of Ref. [42] observed similar behaviors in the extended Skyrme models. Although the correlation between b'_4 and $\Delta F^{\mathrm{Ca48/Pb208}}$ may not be strong, as observed in Ref. [12], b'_4 can be quite sensitive to a linear combination of ΔF^{Ca48} and $\Delta F^{\mathrm{Pb208}}$, such as $a''\Delta F^{\mathrm{Ca48}} + b''\Delta F^{\mathrm{Pb208}}$, and by tuning b'_4, the agreement between theoretical predictions and joint PREX-2/CREX measurements is efficiently improved. However, we realized that in RMF models, the increase of b'_4 usually comes with the amplification of the (isovector) nucleon density fluctuation, altering of single-particle energy spectrum as discussed in Ref. [54], and an increase of g_δ and g_ρ, which break the common quadratic dependence of symmetry energy on asymmetry. The Skyrme/RMF posterior dataset may help in the search of optimized models with more physical constraints in future investigations.

Finally, among numerous RMF models that fall within the 1σ of the PREX-2/CREX, respectively, we identify CPREX1 that maintains good agreement (<1 % deviation) with the binding energy, the charge radii of ^{208}Pb, ^{90}Zr, and ^{48}Ca, as well as tidal deformability and maximum mass of NSs. Similar to DINO with large g_δ and g_ρ, CPREX1 deviates from the quadratic dependence of symmetry energy on isospin asymmetry, yielding $S_{\mathrm{V}} = 32.9$ MeV around SNM, but $S_{\mathrm{V}} = 54.3$ MeV when defined with respect to PNM.

Follow-up neutron skin experiments, like the Mainz Radius EXperiment (MREX), will continue to refine the possible uncertainty of the PREX-2 experiment [55]. The linear relations between the isovector parameters (S_{V}, L, and b'_4) and the ΔF values of ^{208}Pb and ^{48}Ca may serve as a simple "emulator" for rapidly and reliably approximating S_{V}, L, and b'_4 in the investigations of neutron skin thickness experiments.

ACKNOWLEDGMENTS

We acknowledge Jorge Piekarewicz and Jim Lattimer for the helpful discussions during the INT Workshop INT-22R-2A. T.Z. was supported by the Network for Neutrinos, Nuclear Astrophysics and Symmetries, through the National Science Foundation Physics Frontier Center Grant No. PHY-2020275. M.P. and T.Z. acknowledge support by the Department of Energy, Award No. DE-FG02-93ER40756. Z.L. and A.W.S. were supported by NSF PHY 21-16686. A.W.S. was also supported by the Department of Energy Office of Nuclear Physics. B.K. acknowledges partial support from the Anusandhan National Research Foundation, Government of India, with Grant No. CRG/2021/000101.

T.Z. and Z.L. contributed equally to this work.

DATA AVAILABILITY

The data that support the findings of this article are openly available [17]; embargo periods may apply.

APPENDIX A: RELATIVISTIC MEAN-FIELD MODEL AND SKYRME MODEL

In this Appendix, we provide an overview of the theoretical framework utilized. For a more comprehensive understanding, interested readers can refer to the detailed discussions available in various sources such as Refs. [56–58] along with their cited references. The starting point for our relativistic calculation of nuclear response is based on the covariant model presented in Ref. [49]. Additionally, we incorporate the δ meson to accommodate the CREX experiment, which prefers softer symmetry energy [9]. The interacting Lagrangian density can be expressed as

$$\begin{aligned}\mathscr{L}_{\mathrm{int}} = \bar{\psi}\Big[g_\sigma\sigma + \frac{g_\delta}{2}\boldsymbol{\tau}\cdot\boldsymbol{\delta} - \Big(g_\omega\omega_\mu + \frac{g_\rho}{2}\boldsymbol{\tau}\cdot\boldsymbol{\rho}_\mu + \frac{e}{2}(1+\tau_3)A_\mu\Big)\gamma^\mu\Big]\psi \\ - \frac{\kappa}{3!}(g_\sigma\sigma)^3 - \frac{\lambda}{4!}(g_\sigma\sigma)^4 + \frac{\zeta_\omega}{4!}g_\omega^4(\omega_\mu\omega^\mu)^2 + \Lambda_{\omega\rho}\big(g_\rho^2\,\boldsymbol{\rho}_\mu\cdot\boldsymbol{\rho}^\mu\big)\big(g_\omega^2\omega_\nu\omega^\nu\big).\end{aligned} \tag{A1}$$

The Lagrangian density used in our study includes the isodoublet nucleon field ψ as the basic degree of freedom. These nucleons interact via photon (A_μ) exchange and through the exchange of four massive mesons: a scalar-isoscalar (σ), scalar-isovector (δ), a vector-isoscalar (ω^μ), and a vector-isovector (ρ^μ). This formulation is based on the works of Refs. [59–61]. The coupling constant $\Lambda_{\omega\rho}$ for the isoscalar-isovector interaction plays a crucial role in determining the density dependence of the symmetry energy, particularly its slope at saturation density L, as discussed in Ref. [7]. It is noteworthy that the model can be calibrated using an analytical one-to-one correspondence between bulk parameters of infinite nuclear matter and the various coupling constants. Specifically, the values of the symmetry energy S_{V}, its slope L, and curvature K_{sym} at saturation density are correlated to the isovector parameters (g_δ, g_ρ, and $\Lambda_{\omega\rho}$) as explained in Refs. [49,62]. Table II shows the σ meson mass and eight coupling constants for CPREX1 and CPREX2 proposed in this work. The masses of other massive mesons and the free nucleon are $m_\delta = 980$ MeV, $m_\omega = 782.5$ MeV, $m_\rho = 763$ MeV, and

$m = 939$ MeV. The nuclear properties of ^{48}Ca and ^{208}Pb are shown in Table III, along with experimental measurement and our Hartree calculations for various models for comparison. These two nuclei, together with ^{90}Zr (not shown), are selected for inclusion in our Bayesian likelihood to limit computational cost, as the evaluation of finite nuclei properties constitutes the main bottleneck in the sampling. While the CPREX models reproduce the binding energies and charge radii of these nuclei with high accuracy, they are not optimized for global nuclear fits. For example, the binding energy per nucleon of ^{16}O for CPREX1 is predicted with an error of about 2%, which, while larger than for the nuclei included in the fit, remains competitive with or better than the uncertainty range of chiral EFT (1–10%). We emphasize that prioritizing consistency with PREX2/CREX and astrophysical constraints necessarily limits the model's ability to fit additional nuclei, given its finite degrees of freedom. Fitting to a broader range of nuclei would risk overfitting and reduce the sensitivity to the observables we aim to constrain. Table IV shows the infinite nuclear matter properties at saturation density and the neutron star properties calculated from EOSs in β equilibrium. The crust EOSs are constructed with the compressible liquid droplet model with fixed surface tension parameters $\sigma_s = 1.2$ MeV fm^{-2} and $S_S = 48$ MeV [67]. The tabulated complete EOSs of these RMF models can be found in the GitHub repository [17].

To gain a complementary understanding of both PREX-2/CREX measurements, we also study the Skyrme interactions inferred from those neutron skin thickness measurements. The Skyrme Hamiltonian for infinite nuclear matter is written as

$$H_{\rm Sk} = \frac{k_{Fn}^5}{10\pi^2 m_n^*} + \frac{k_{Fp}^5}{10\pi^2 m_p^*} + H_{\rm pot}(n_n, n_p), \tag{A2}$$

where the first two terms are the kinetic terms for the neutrons and the protons with effective mass contribution and $H_{\rm pot}$ is the potential term expressed as

$$H_{\rm pot} = \frac{1}{2}n^2 t_0\left(1+\frac{x_0}{2}\right) - \frac{1}{2}\left(n_n^2+n_p^2\right)t_0\left(\frac{1}{2}+x_0\right) + \frac{1}{24}n^\gamma t_3\left(n^2(2+x_3) - \left(n_n^2+n_p^2\right)(1+2x_3)\right). \tag{A3}$$

The neutron and proton effective masses are functions of densities as

$$\frac{m_{n/p}}{m_{n/p}^*} = 1 + \frac{m_{n/p}}{4}\{n[t_1(2+x_1)+t_2(2+x_2)] + n_{n/p}[-t_1(1+2x_1)+t_2(1+2x_2)]\}. \tag{A4}$$

To describe a finite nucleus, two additional terms are included in the Skyrme Hamiltonian [38,43]. These terms are

$$H_{\rm SO} = b_4 \mathbf{J}\cdot\nabla n + b_4'(\mathbf{J}_n\cdot\nabla n_n + \mathbf{J}_p\cdot\nabla n_p) \tag{A5}$$

and

$$H_{\rm J} = -\tfrac{1}{16}(t_1x_1+t_2x_2)\mathbf{J}^2 + \tfrac{1}{16}(t_1-t_2)\left(\mathbf{J}_n^2+\mathbf{J}_p^2\right), \tag{A6}$$

where $H_{\rm SO}$ are spin-orbit interactions and $H_{\rm J}$ are the central tensor terms. The $\mathbf{J}_{n/p}$ is the spin-orbit density $\mathbf{J}_{n/p} = \psi_{n/p}^\dagger \overrightarrow{\sigma} \times \overrightarrow{\nabla}\psi_{n/p}$ and $\mathbf{J} = \mathbf{J}_n + \mathbf{J}_p$.

APPENDIX B: THE APPROXIMATED SPIN-ORBIT POTENTIAL IN RMF MODELS

The large component of the Dirac equation follows

$$\left[\vec{\sigma}\cdot\vec{p}\frac{1}{2m+\epsilon-S-V}\vec{\sigma}\cdot\vec{p} - S + V\right]g(r) = \epsilon g(r), \tag{B1}$$

where $S = g_\sigma\,\sigma_0 \pm g_\delta\delta_0$ and $V = g_\omega\,\omega \pm g_\rho\rho_0$ are mean-field potentials from classical expectation value of meson fields. By reducing the spherically symmetric Dirac equation with scalar and vector potentials to the nonrelativistic Schrödinger equation to order $(p/m)^2$ [68,69], the effective single nucleon classical Hamiltonian is

$$H = \vec{p}\frac{1}{2M^*}\vec{p} - S(r) + V(r) + V_{\rm SO}\vec{s}\cdot\vec{l}, \tag{B2}$$

$$V_{\rm SO} = -\frac{1}{r}\frac{d}{dr}\left[\frac{1}{M^*}\right], \tag{B3}$$

where $\vec{l} = \vec{r}\times\vec{p}$, $\vec{s} = \vec{\sigma}/2$, and M^* could be defined as the Dirac mass $M^D = m - S(r)$ assuming that the relativistic single-particle energy $\epsilon + S(r) - V(r) \ll 2(m-S)$. However, it is possible to rearrange terms of higher order in $(p/m)^2$ to obtain an equivalent form, $M^* = m - V(r)$, as shown in the Appendix of Ref. [69]. Although these two expressions are equivalent to order $(p/m)^2$, their ratio can be on the order of 10%, as $S(0) - V(0) \approx 50$ MeV, the empirical depth of the nucleon potential well. Therefore, we consider the average of these two choices originally introduced in Ref. [6],

$$M^* = m - \frac{S(r)+V(r)}{2}, \tag{B4}$$

which can also be justified by taking $\epsilon \ll 2m - S - V$ [70,71]. Note that this definition of M^* should not be confused with the Dirac or Landau effective mass. Our qualitative conclusions remain unchanged regardless of the specific definition of M^* used. Since scalar and vector potentials are mainly determined by the corresponding densities of the two-form current, modified by Coulomb interaction and the self- and mixing couplings of mesons, we can simplify by considering only Yukawa coupling to generate the potentials. Furthermore, vector densities are strongly correlated with scalar densities, allowing us to approximate scalar densities with vector densities:

$$S(r) = \frac{g_\sigma^2}{m_\sigma^2}n_B \pm \frac{g_\delta^2}{4m_\delta^2}(n_p - n_n), \tag{B5}$$

$$V(r) = \frac{g_\omega^2}{m_\omega^2}n_B \pm \frac{g_\rho^2}{4m_\rho^2}(n_p - n_n), \tag{B6}$$

where the upper sign is for protons and the lower sign is for neutrons. The difference of isospin potential between proton and neutron is

$$V_{\rm SO}^p + V_{\rm SO}^n = -\frac{d}{rdr}\left[\frac{M_p^* + M_n^*}{M_p^* M_n^*}\right], \tag{B7}$$

TABLE III. Experimental data for the binding energy per nucleon [63], charge radii [64], neutron skins (excluding PREX-2/CREX) [65], charge form factor, and form factor difference from PREX [8] for ^{208}Pb and CREX [9] for ^{48}Ca. Also displayed are the theoretical results obtained with NL3 [1], FSUGold2 [49], IOPB-I [56], IUFSU [50], BigApple [66], HPUC [51], BSRV [52], DINOa–c [10], and the two parametrizations, CPREX1 and CPREX2.

		Experiment	NL3	FSU2	IOPB-I	IUFSU	BigApple	HPUC	BSRV	DINOa	DINOb	DINOc	CPREX1	CPREX2
	B/A (MeV)	7.87	7.88	7.87	7.86	7.88	7.85	7.85	7.84	7.87	7.87	7.87	7.84	7.86
	$R_{\rm ch}$ (fm)	5.50	5.51	5.49	5.52	5.49	5.50	5.56	5.53	5.51	5.51	5.51	5.49	5.49
^{208}Pb	$\Delta R_{\rm np}$ (fm)	0.159 ± 0.017	0.2797	0.2862	0.2195	0.1618	0.1508	0.1196	0.2595	0.1746	0.1993	0.2235	0.1905	0.1525
	$F_{\rm ch}$	0.409	0.4067	0.4094	0.4052	0.4106	0.4080	0.3992	0.4043	0.4074	0.4075	0.4073	0.4100	0.4092
	ΔF	0.041 ± 0.013	0.0414	0.0423	0.0319	0.0233	0.0214	0.0168	0.0378	0.0262	0.0303	0.0342	0.0282	0.0222
	B/A (MeV)	8.67	8.65	8.62	8.64	8.53	8.52	8.65	8.66	8.67	8.67	8.67	8.64	8.66
	$R_{\rm ch}$ (fm)	3.48	3.45	3.43	3.45	3.44	3.46	3.46	3.44	3.47	3.47	3.47	3.48	3.46
^{48}Ca	$\Delta R_{\rm np}$ (fm)	0.137 ± 0.015	0.2255	0.2318	0.1995	0.1736	0.1690	0.1479	0.2196	0.0994	0.1054	0.1141	0.1252	0.1357
	F_{ch}	0.158	0.1604	0.1665	0.1616	0.1647	0.1582	0.1577	0.1621	0.1591	0.1589	0.1585	0.1537	0.1571
	ΔF	0.0277 ± 0.0055	0.0551	0.0564	0.0490	0.0435	0.0413	0.0391	0.0527	0.0330	0.0345	0.0364	0.0335	0.0362

TABLE IV. Saturation properties and neutron star properties of RMF models listed in Table III. Saturation properties for SNM and PNM are defined in Sec. II. For all models except DINOa–c and CPREX1–2, the two definitions coincide. In these cases, the discrepancy signals the breakdown of the quadratic approximation of symmetry energy. Neutron star properties are calculated with the crust EOSs constructed with the compressible liquid droptlet model, repectively, for various RMF models with fixed surface tension parameters $\sigma_s = 1.2$ MeV fm^{-2} and $S_S = 48$ MeV [67].

		NL3	FSU2	IOPB-I	IUFSU	BigApple	HPUC	BSRV	DINOa	DINOb	DINOc	CPREX1	CPREX2
	n_s (fm^{-3})	0.1483	0.1504	0.1495	0.1546	0.1546	0.1490	0.1480	0.1522	0.1525	0.1519	0.1516	0.1518
	M^D (MeV)	558.7	557.0	557.2	572.1	572.8	572.9	565.3	587.4	593.0	593.9	692.8	648.1
	B (MeV)	16.24	16.26	16.10	16.40	16.34	15.98	16.10	16.16	16.21	16.21	16.29	16.14
SNM	K (MeV)	271.6	237.7	222.6	231.3	227.0	220.2	227.2	210.0	207.0	206.0	223.8	223.5
	S_V (MeV)	37.3	37.6	33.3	31.3	31.3	28.4	36.1	31.4	33.1	34.6	32.9	29.8
	L (MeV)	118.2	112.7	63.6	47.2	39.8	41.6	84.6	50.0	70.0	90.0	−3.5	0.4
	K_{sym} (MeV)	101.0	25.4	−37.0	28.5	87.5	81.1	−73.2	506.0	609.1	714.8	−418.4	−239.8
	M_n^D (MeV)	569.2	566.0	566.7	580.5	582.8	581.4	573.3	352.1	333.0	320.5	377.4	465.6
	M_p^D (MeV)	569.2	566.0	566.7	580.5	582.8	581.4	574.8	908.8	948.2	969.1	1062.5	870.1
PNM	S_V (MeV)	38.3	38.6	34.7	32.9	33.1	29.9	37.2	46.5	50.6	53.4	54.3	38.4
	L (MeV)	121.2	115.9	67.7	49.5	40.6	42.7	88.7	172.1	216.4	247.8	211.2	75.9
	K_{sym} (MeV)	100.3	27.2	−45.5	23.1	74.3	89.2	−70.6	726.7	907.2	1021.2	801.8	76.4
	M_{max} ($M_\odot$)	2.77	2.07	2.15	1.94	2.60	2.05	2.04	2.17	2.15	2.15	2.04	2.12
	$R_{1.0}$ (km)	14.4	14.1	13.2	12.6	12.8	12.6	13.6	14.4	14.8	15.1	13.9	12.9
NS	$R_{1.4}$ (km)	14.5	13.9	13.2	12.6	13.1	12.8	13.4	14.4	14.6	14.9	13.4	12.9
	$\Lambda_{1.0}$	7797	6473	4347	3384	3918	3752	4903	6623	7572	8579	4543	3544
	$\Lambda_{1.4}$	1275	876	687	500	719	593	689	1065	1150	1256	584	570

$$V_{\rm SO}^{p} - V_{\rm SO}^{n} = \frac{d}{rdr}\left[\frac{M_p^* - M_n^*}{M_p^* M_n^*}\right], \tag{B8}$$

$$M_p^* - M_n^* = -\left(\frac{g_\delta^2}{m_\delta^2} + \frac{g_\rho^2}{m_\rho^2}\right)\frac{n_p - n_n}{4}, \tag{B9}$$

$$M_p^* + M_n^* = 2m - \left(\frac{g_\sigma^2}{m_\sigma^2} + \frac{g_\omega^2}{m_\omega^2}\right)n_B, \tag{B10}$$

since $(M_p^* + M_n^*)^2 \gg (M_p^* - M_n^*)^2$, we can take $M_p^* M_n^* \approx (M_p^* + M_n^*)^2/4$, keeping only linear term in vector densities,

$$V_{\rm SO}^{p} + V_{\rm SO}^{n} \approx -\frac{\frac{g_\sigma^2}{m_\sigma^2} + \frac{g_\omega^2}{m_\omega^2}}{rm^2}\frac{dn_B}{dr}, \tag{B11}$$

$$V_{\rm SO}^{p} - V_{\rm SO}^{n} \approx -\frac{\frac{g_\delta^2}{m_\delta^2} + \frac{g_\rho^2}{m_\rho^2}}{4rm^2}\frac{d(n_p - n_n)}{dr}. \tag{B12}$$

A similar form without the δ meson has been used to study the isospin dependence of the spin-orbit interaction, contrasting with the spin-orbit force in nonrelativistic Skyrme models [72–74]. Isospin dependence of spin-orbit interaction is introduced to Skyrme models as

$$V_{\rm SO}^{p/n} = -\frac{2b_4}{r}\frac{dn_B}{dr} - \frac{b_4'}{r}\frac{d}{dr}[n_B \pm (n_p - n_n)] \tag{B13}$$

to address the problem of isotope shifts in the Pb region [38]. Note that in older models with only one spin-orbit potential parameter, $W_0 = 2b_4 = 2b_4'$ is about 100 MeV fm^{-5}[44,74].

$$V_{\rm SO}^{p} + V_{\rm SO}^{n} = -\frac{4b_4 + 2b_4'}{r}\frac{dn_B}{dr}, \tag{B14}$$

$$V_{\rm SO}^{p} - V_{\rm SO}^{n} = -\frac{2b_4'}{r}\frac{d}{dr}[n_p - n_n]. \tag{B15}$$

By comparing Eqs. (B14) and (B15) with Eqs. (B11) and (B12), the model parameter b_4 and b_4' can be expressed as

$$b_4 \approx \frac{1}{4m^2}\left(\frac{g_\sigma^2}{m_\sigma^2} + \frac{g_\omega^2}{m_\omega^2} - \frac{g_\delta^2}{4m_\delta^2} - \frac{g_\rho^2}{4m_\rho^2}\right), \tag{B16}$$

$$b_4' \approx \frac{1}{8m^2}\left(\frac{g_\delta^2}{m_\delta^2} + \frac{g_\rho^2}{m_\rho^2}\right). \tag{B17}$$

In RMF models, we obtain b_4 and b_4' similar to those in nonrelativistic models, as described in the above equations. In principle, b_4 and b_4' are density dependent in RMF models. We take the leading order term so that b_4 and b_4' are essentially a linear combination of Yukawa coupling strength.

APPENDIX C: WEAK CHARGE FORM FACTORS WITH SPIN-ORBIT CONTRIBUTIONS

Form factors are key observable in electron scattering experiments. To calculate the weak charge form factor measured in PREX-2/CREX, we perform finite nuclei calculations to obtain the proton and neutron profiles, and then perform Fourier transform on the profile to get the corresponding form factor. In this work, we consider the impact of spin-orbit currents on the electromagnetic and weak charge form factors of ^{48}Ca and ^{208}Pb. It has been shown that the contributions from spin-orbit currents are comparable to the present CREX experimental error bars [39], and therefore it should be necessary to incorporate spin-orbit currents in the calculation of weak form factors as

$$ZF_{\rm ch}(q) = \sum_{i=p,n}\left\{G_{\rm E}^i(q^2)F_{\rm V}^i(q) + \frac{G_{\rm M}^i(q^2) - G_{\rm E}^i(q^2)}{1+\tau} \times \left[\tau F_{\rm V}^i(q) + \frac{q}{2m}F_{\rm T}^i(q)\right]\right\}$$

and

$$Q_W F_W(q) = \sum_{i=p,n}\left\{\tilde{G}_{\rm E}^i(q^2)F_{\rm V}^i(q) + \frac{\tilde{G}_{\rm M}^i(q^2) - \tilde{G}_{\rm E}^i(q^2)}{1+\tau} \times \left[\tau F_{\rm V}^i(q) + \frac{q}{2m}F_{\rm T}^i(q)\right]\right\},$$

where $\tau = q^2/4m^2$, the $G_{\rm E,M}^i$ are electric and magnetic single nucleon form factors, and the $\tilde{G}_{\rm E,M}^i$ are electric and magnetic form factors for the weak-neutral current. Similar to Ref. [39], we adopted a simple dipole parametrization of these single-nucleon form factors.

The vector and tensor form factors $F_{\rm V}(q)$ and $F_{\rm T}(q)$ are obtained by

$$F_{\rm V}(q) = \sum_{n\kappa}(2j+1)\int_0^\infty \left[g_{n\kappa}^2(r) + f_{n\kappa}^2(r)\right]j_0(qr)dr$$

and

$$F_{\rm T}(q) = \sum_{n\kappa}2(2j+1)\int_0^\infty g_{n\kappa}(r)f_{n\kappa}(r)j_1(qr)dr\ ,$$

where $g_{n\kappa}(r)$ and $f_{n\kappa}(r)$ are the upper and lower components of Dirac spinor in RMF models. Wavefunctions in the nonrelativistic Skyrme model correspond to the larger upper component $g_{n\kappa}(r)$. The lower component $f_{n\kappa}(r)$ is obtained by assuming a free space relation [9,39]:

$$f_{n\kappa}(r) = \frac{1}{2m}\left(\frac{d}{dr} + \frac{\kappa}{r}\right)g_{n\kappa}(r).$$

APPENDIX D: BAYESIAN ANALYSIS

1. Prior

In this appendix, we describe the prior, likelihood, and posterior in our Bayesian analysis. Our RMF model has 12 parameters. We fixed the δ, ω, and ρ meson masses at $m_\delta = 980$ MeV, $m_\omega = 782.5$ MeV, and $m_\rho = 763$ MeV, as in many FSU-type models [49], leaving us with nine free parameters. The σ meson mass is a free parameter with a uniform distribution in the range [450, 550] MeV, corresponding to mass of $f_0(500)$ [78]. We also take a uniform prior for the SNM properties n_s, B, M^D, and K, as shown in Table V. These four bulk nuclear properties can be mapped to four isoscalar coupling constants, as in Ref. [49], except for the ω meson self-coupling ζ_ω, which takes a flat distribution in the range [0, 0.03], since $\zeta_\omega > 0.03$ is suppressed by astronomical observations [79], particularly due to the maximum-mass constraint. The isovector sector

TABLE V. Prior distribution of Skyrme and RMF parameters. n_s, B, m^* (or M^D), K, and S_V map to t_0, t_1, t_2, t_3, and γ for Skyrme models and g_σ, g_ω, g_ρ, κ, and λ for RMF models.

	Parameter	Prior
	n_s (MeV)	[0.14, 0.165] [35]
	B (MeV)	[−15.5, −16.5] [35]
Both	m^*, M^D (MeV)	[0.5,0.8]×939 [75]
	K (MeV)	[210, 250] [76]
	S_V (MeV)	[20, 50] [77]
	m_σ (MeV)	[450, 550]
	m_δ (MeV)	980
	m_ω (MeV)	782.5
RMF	m_ρ (MeV)	763
	L (MeV)	$[L^-, L^+]$
	g_δ^2	[0, 1500]
	ζ_ω	[0, 0.03]
	x_0	[−1.81, 2.15]
	x_1	[−7.53, 3.77]
Skyrme	x_2	[−49.90, 91.93]
	x_3	[−3.41, 3.73]
	b_4 (fm^4)	[−0.36, 0.72]
	b'_4 (fm^4)	[−0.36, 0.72]

is governed by g_δ, g_ρ, and $\Lambda_{\omega\rho}$, which can be mapped to the symmetry energy properties S_V and L, assuming a flat distribution of g_δ in the range [0, 1500], covering higtest value in DINO models [10]. S_V takes a uniform prior, while L is uniformly distributed in $[L^-, L^+]$. Because L^- and L^+ are not fixed but determined by other parameters, the flat distributions of these parameters result in a nonflat prior distribution of L:

$$P(L) = \int_{\zeta_\omega^-}^{\zeta_\omega^+} \cdots \int_{m_\sigma^-}^{m_\sigma^+} \int_{L^-(m_\sigma,\ldots,\zeta_\omega)}^{L^+(m_\sigma,\ldots,\zeta_\omega)} \delta(L' - L) dL' dm_\sigma \cdots d\zeta_\omega. \tag{D1}$$

L^- is a physical bound beyond which the quadratic formula for mapping L to $\Lambda_{\omega\rho}$ has no solution [49]. L^+ can be solved by setting $\Lambda_{\omega\rho} = 0$, so that $L < L^+$ corresponds to $\Lambda_{\omega\rho} > 0$, ensuring that β-equilibrium matter remains neutron-rich ($n_p < n_n$) at high density. Positive $\Lambda_{\omega\rho}$ is introduced to reduce the symmetry energy, similar to the positive ζ_ω, which serves to reduce the SNM energy. Thus, we take $\Lambda_{\omega\rho} = 0$ as our natural upper bound for the symmetry energy slope in the RMF model.

The prior distribution of Skyrme parameters is chosen similarly to ensure consistency with the prior distribution used for the RMF models. We use flat prior distributions for n_s, B, m^*, K, and S_V, as well as for the x_i, b_4, and b'_4 parameters with bounds in Table V. The range of the x_i, b_4, and b'_4 parameters in the Skyrme prior distributions is determined as follows. First, we examined 11 widely used Skyrme models (SGII [80], NRAPR [27], UNEDF0 [81], UNEDF2 [34], SLy4 , SV-min [46], SkO [82], SkOp [83], BSk16 [84], KDE0v [85], and Gs [86]). We then identified the maximum and minimum x_i, b_4, and b'_4 parameters in these 11 models, denoted as $x_i^{\max}$, $x_i^{\min}$, $b_4^{\max}$, $b_4^{\min}$, $b_4'^{\max}$, and $b_4'^{\min}$. To cover a wide range of possible Skyrme parameters, we determine the prior distribution of x_i, b_4, and b'_4 parameters as $[x_i^{\min} - \Delta x_i, x_i^{\max} + \Delta x_i]$, $[b_4^{\min} - \Delta b_4, b_4^{\max} + \Delta b_4]$, and $[b_4'^{\min} - \Delta b'_4, b_4'^{\max} + \Delta b'_4]$, where $\Delta x_i = x_i^{\max} - x_i^{\min}$, $\Delta b_4 = b_4^{\max} - b_4^{\min}$, and $\Delta b'_4 = b_4'^{\max} - b_4'^{\min}$.

TABLE VI. The list of experimental properties with adopted uncertainties. The binding energy per nucleon [63] and charge radii [64] are included. Charge and weak form factor F_{ch} and F_W listed here correspond to momentum transfer $q = 0.8733\,\text{fm}^{-1}$ for ^{48}Ca in CREX [9] or $0.3977\,\text{fm}^{-1}$ for in PREX [8].

	Property	Mean	Standard deviation
	$R_{ch}^{^{48}Ca}$ (fm)	3.48	0.070
	$R_{ch}^{^{90}Zr}$ (fm)	4.27	0.085
	$R_{ch}^{^{208}Pb}$ (fm)	5.50	0.11
Basic nuclei	$B/A^{^{48}Ca}$ (MeV)	8.67	0.433
constraints	$B/A^{^{90}Zr}$ (MeV)	8.71	0.436
	$B/A^{^{208}Pb}$ (MeV)	7.87	0.393
	$F_{ch}^{^{48}Ca}$	0.1581	0.005
	$F_{ch}^{^{208}Pb}$	0.409	0.005
CREX	$F_W^{^{48}Ca} - F_{ch}^{^{48}Ca}$	0.0277	0.0055
PREX	$F_W^{^{208}Pb} - F_{ch}^{^{208}Pb}$	0.041	0.013

Additionally, we constrain our RMF and Skyrme models to ensure that the pressure of matter in β equilibrium is always increasing with increasing energy density and to ensure that the proton fraction in β equilibrium never vanishes. Note that this does not guarantee that symmetry energy slope L defined around SNM has to be positive.

2. Likelihood

In the Bayesian analysis of RMF and Skyrme models, we use the same constraints and uncertainties. To account for theoretical uncertainty, we incorporate a 2% uncertainty in the measured value of R_{ch} and a 5% uncertainty in the standard deviation of B/A. It is also necessary to constrain F_{ch} accurately to ensure that the electric weak form factor difference, $F_{ch} - F_W$, can be interpreted as a measurement in PREX-2/CREX. The constraints on B/A, R_{ch}, and F_{ch} together form the basic nuclear constraints in our Bayesian analysis, as listed in Table VI.

Sampling with basic nuclear constraints results in drastically different posteriors for L. In the Skyrme model, negative L is suppressed by the constraint that the pressure of matter in β equilibrium is always increasing with energy density. However, RMF models with negative L around SNM can have a large symmetry energy slope around PNM due to the breakdown of the quadratic formula of symmetry energy with large g_δ and g_ρ. Since our goal is not to constrain the nuclear model with basic nuclear constraints, we add a likelihood factor to our RMF models to ensure the S_V-L distribution is compatible between Skyrme and RMF models with only basic nuclei constraints, as shown by the horizontally shaded ellipse in Fig. 1.

In addition to the basic nuclear constraints, we impose additional PREX-2/CREX constraints separately and jointly, forming four sets of likelihoods: basic nuclei, +PREX, +CREX, and +PREX + CREX. We take the electric weak form factor difference $F_{ch} - F_W$ instead of the weak form

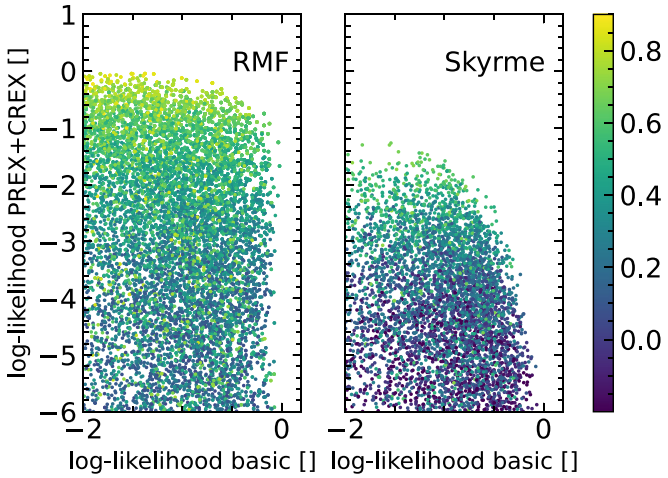


FIG. 4. The likelihood posterior samples of Skyrme and RMF models colored by the parameter b'_4 from -0.36 (deep blue) to 0.9 (yellow) fm^4. The x axis shows the log-likelihood from basic nuclei constraints including binding energy, charge radii, and charge form factor, while the y axis shows the log-likelihood of PREX-2/CREX experiments in Table VI.

factor F_W as constraints of PREX-2/CREX experiments, as tabulated in Table VI. In principle, the weak form factor F_W can be determined from the parity-violating asymmetry $A_{\rm PV}$ measured in PREX-2/CREX experiments through Coulomb distortion calculations, assuming an electric charge distribution. Since the electric charge distribution has already been determined experimentally with great accuracy, both F_W and $F_{\rm ch} - F_W$ are determined experimentally from the measured $A_{\rm PV}$ without any model dependence. However, theoretical models like RMF and Skyrme models, optimized with charge radius, do not have enough accuracy to ensure consistency with the charge distribution assumed in Coulomb distortion calculations. Therefore, we need to make sure that the value of $F_{\rm ch}$ used in our calculations is close to that used in the analysis of PREX-2/CREX. To achieve this, we take $\sigma_{F_{\rm ch}} = 0.005$, which is much smaller than σ_{F_W}. Due to the remaining uncertainty in $F_{\rm ch}$, we consider $F_{\rm ch} - F_W$ in the likelihood of its better constraints compared to F_W.

Figure 4 shows the likelihood of basic nuclei constraints versus the likelihood of PREX-2/CREX experiments listed in Table. VI. The lack of points in the upper right corner indicates the tension between basic nuclei properties and the PREX-2/CREX results. The fact that the points close to the upper right corner all have relatively large b'_4 indicates that larger b'_4 in mean-field models may mitigate the tension between basic nuclei constraints and the PREX-2/CREX experiments.

Finally, we want to comment on additional constraints from giant monopole resonances (GMRs) and dipole polarizability, which we do not consider explicitly in the likelihood. Instead, we use a tight prior on the compressibility K within the empirical window [210, 250] MeV to account for GMR. Although we do not include dipole polarizability explicitly, it is possible to consider dipole polarizability as an additional independent constraint on $S_{\rm V}$ [33]:

$$S_{\rm V} = \frac{L + [146 \pm 1]\,{\rm MeV}}{[6.11 \pm 0.316]}. \tag{D2}$$

This is shown in Fig. 1 and applied in Fig. 2.

3. Posterior

With the prior and likelihood discussed above, we obtain the posterior distributions of model parameters, saturation properties, and ΔF measured in PREX-2/CREX, as shown in Figs. 5 and 6. To highlight the significant aspects of the posterior distribution, we also plot the Pearson correlation coefficient between any two parameters, as shown in the upper right corner of Figs. 5 and 6. Some model parameters, such as t_0, t_3, and $\alpha = \gamma - 2$, are tightly correlated due to the mapping between saturation properties used in our prior. Isoscalar and isovector Yukawa couplings are also tightly correlated due to the priors on binding energy B and effective mass M^*. For both Skyrme and RMF models, the symmetry energy $S_{\rm V}$ and its slope L are very sensitive parameters related to the form factor difference measured in PREX-2/CREX. From the posterior of Bayesian analysis, we obtain the mean and covariance of $S_{\rm V}$ and L with +PREX + CREX constraints,

$$(\bar{S}_{\rm V}, \bar{L}) = (34.1,\ 40.3)_{\rm Skyrme},\ (31.4,\ 49.1)_{\rm RMF}$$
$$\sqrt{\rm cov} = \begin{pmatrix} 6.5 & 9.1 \\ 9.1 & 21.3 \end{pmatrix}_{\rm Skyrme}, \begin{pmatrix} 5.2 & 9.6 \\ 9.6 & 27.4 \end{pmatrix}_{\rm RMF}, \tag{D3}$$

compared with the posterior with basic nuclei constraints only,

$$(\bar{S}_{\rm V}, \bar{L}) = (32.8,\ 66.8),\ \sqrt{\rm cov} = \begin{pmatrix} 5.9 & 11.7 \\ 11.7 & 31.2 \end{pmatrix}. \tag{D4}$$

Interestingly, despite the weak correlation between b'_4 and $\Delta F^{\rm Ca48/Pb208}$ in the Skyrme model, as observed in Ref. [12], b'_4 can be quite sensitive to a linear combination of $\Delta F^{\rm Ca48}$ and $\Delta F^{\rm Pb208}$, such as $a''\Delta F^{\rm Ca48} + b''\Delta F^{\rm Pb208}$, significantly influencing the distribution of $\Delta F^{\rm Ca48}$, $\Delta F^{\rm Pb208}$. The posterior for b'_4 increases to $b'_4 = 0.310^{+0.24}_{-0.26}$ with additional PREX-2/CREX constraints from $b'_4 = 0.244^{+0.21}_{-0.19}$ with basic nuclei constraints only. A similar trend is also observed in RMF models. The detailed impact of b'_4 on the nucleon distribution is discussed in Appendix F below.

Figure 7 shows the finite nuclei properties of ^{48}Ca, ^{90}Zr, and ^{208}Pb of the Bayesian posterior samples with +PREX + CREX constraints. This distribution is consistent with the likelihood imposed in Table VI, with the exception that the charge posterior is more constrained than the 2% charge radius constraints we impose. This tighter constraint on charge radius is indeed due to the charge form factor being more constraining. We also noticed a much weaker $\Delta R_{\rm np}$-ΔF correlation in ^{48}Ca than in ^{208}Pb, since the momentum transfer of electron elastic scattering is much higher in CREX than in PREX due to the experimental setup. Therefore, CREX should be viewed more as a measurement of form factor difference than the neutron skin of ^{48}Ca.

We do not expect isoscalar parameters, such as binding energy B, incompressibility K, self-coupling of ω meson, and ζ, being sensitive to PREX and CREX, which probes isovector properties. Therefore, their posterior is relatively flat as in the

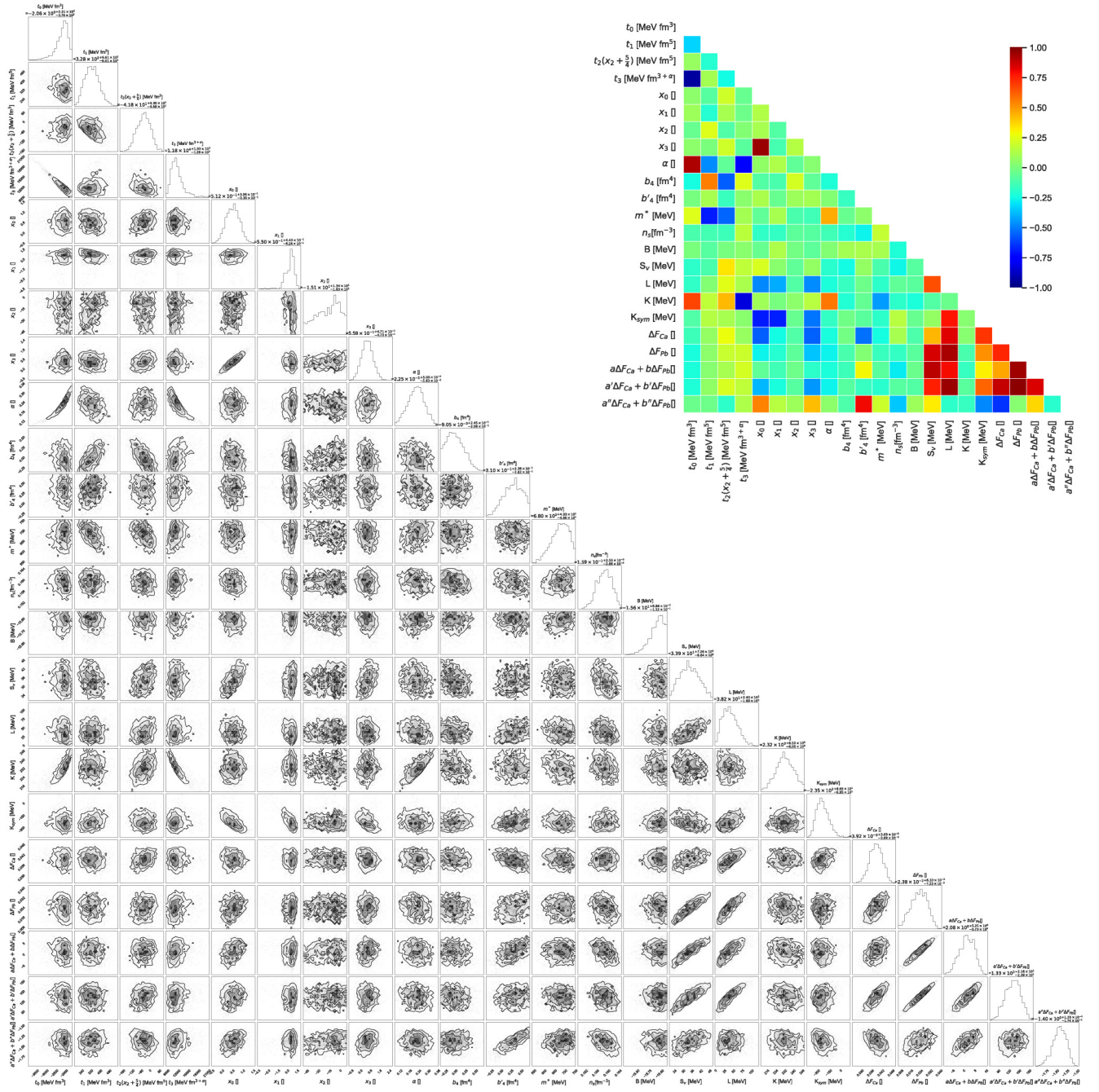


FIG. 5. The posterior distributions of model parameters, saturation properties, and ΔF measured in PREX-2/CREX for Skyrme model. The Pearson correlation coefficient between each pair of variables is displayed in the upper right corner.

prior. $\Lambda_{\omega\rho}$ represents meson mixing between the two vector mesons. Therefore, it is extremely correlated with the Yukawa coupling of the two vector mesons. The meson mixing is small when Yukawa couplings of the two vector mesons are large.

4. Confidence level

The aim of this Appendix is to quantify the level of consistency between theoretical predictions of ΔF for ^{48}Ca and ^{208}Pb, derived from Skyrme and RMF models, and the experimental measurements reported by PREX-2/CREX. This is accomplished using the well-established statistical framework of confidence levels, which quantify the degree to which measurements are compatible with existing knowledge.

Let us assume that the state of knowledge prior to the CREX measurement suggests $\Delta F^{^{48}\mathrm{Ca}} = 0.0432 \pm 0.01$. Under this assumption, we expect that approximately 68% of subsequent measurements will fall within the 1σ confidence interval: $\Delta F^{^{48}\mathrm{Ca}} \in [0.0332, 0.0532]$, assuming the knowledge is correct. Suppose an experiment yields $\Delta F^{^{48}\mathrm{Ca}} = 0.0332$, which lies exactly at the lower bound of the 1σ interval. In that case, the probability that the current theoretical knowledge

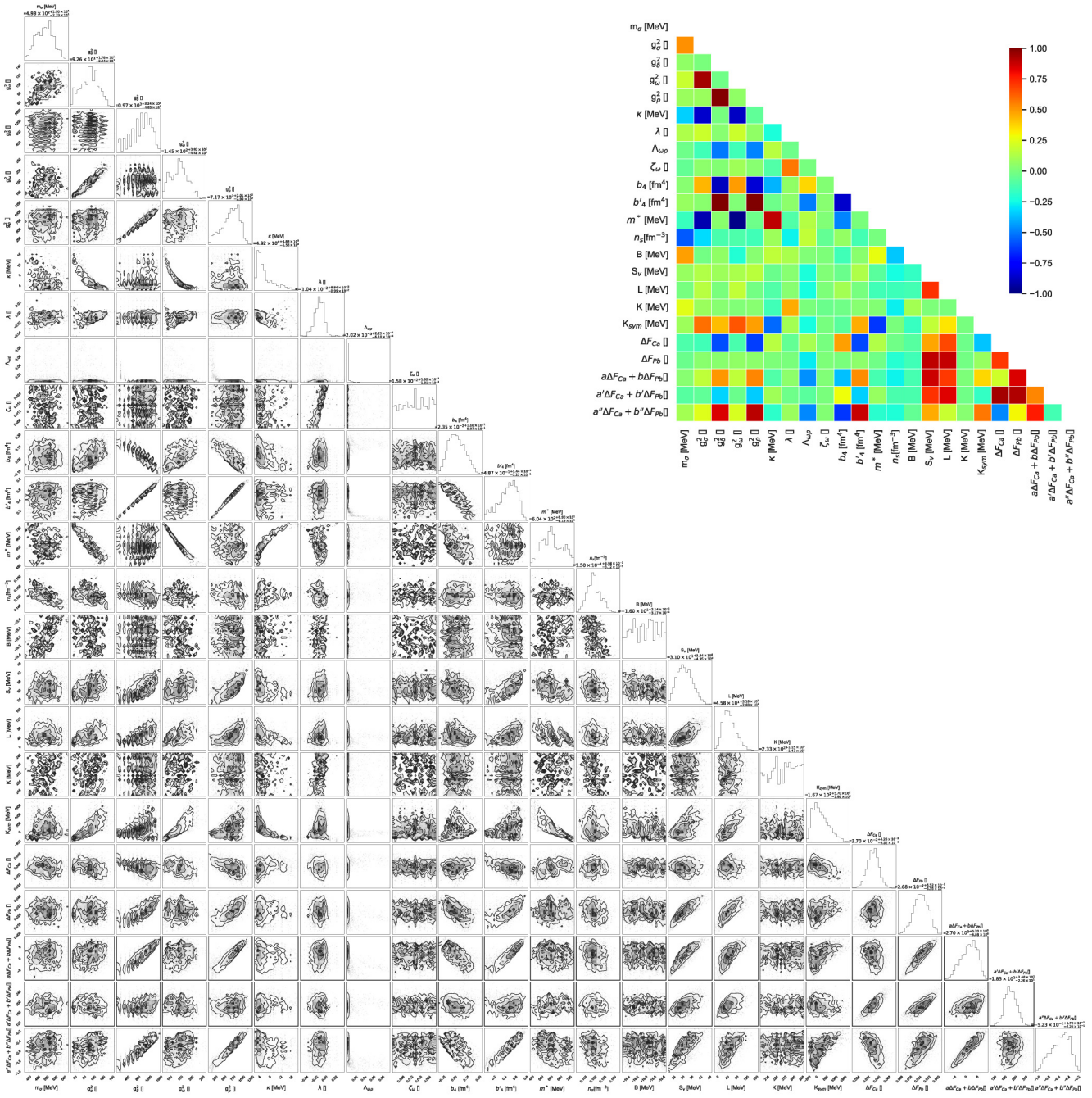


FIG. 6. The same as Fig. 5 but for RMF model.

is correct, given the measurement, is 68%, while there is a 32% probability that the result is a statistical fluctuation inconsistent with the model—this defines the 1σ confidence level. Now, consider CREX measurement with error bar yields $\Delta F^{^{48}\mathrm{Ca}} = 0.0277 \pm 0.0055$. This result lies outside the original 1σ bound, and its 1σ upper bound barely overlaps with the 1σ lower bound of the theoretical expectation. It is a common misconception that such a scenario is equivalent to the prior one. Indeed, the right approach involves computing the difference between the experimental result and the theoretical prediction as a probability distribution: $\mathcal{N}(\mu = 0.0432 - 0.0277, \sigma = \sqrt{0.01^2 + 0.0055^2})$. The null hypothesis (i.e., that the discrepancy is due to statistical fluctuation) corresponds to zero deviation. In this case, zero lies approximately 1.36 standard deviations away from the mean of the difference distribution, implying a p value (significance) of 17.6%. In other words, there is an 82.4% confidence level that the measurement is inconsistent with prior knowledge, once uncertainties are fully accounted for.

The previous example is straightforward because both knowledge and measurement are modeled as Gaussian distributions, and only a single observable is involved. For more general cases—arbitrary distributions with n-dimensional observables $\vec{x}$, we need to perform an overlapping integral to

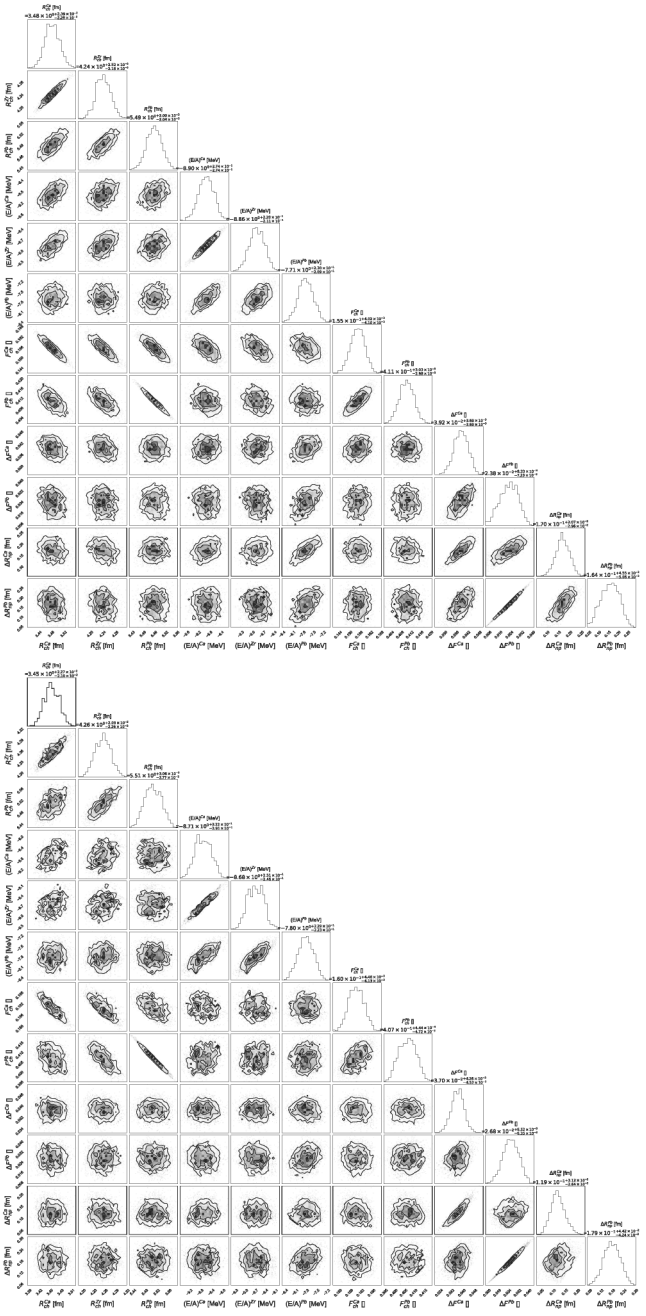


FIG. 7. The posterior distributions of basic nuclear properties used in the likelihood as well as neutron skins of ^{48}Ca and ^{208}Pb for Skyrme model (upper) and RMF (lower) model.

determine how confident level of our knowledge $P_1(\vec{x})$ is correct, given the measurement $P_2(\vec{x})$. Bayesian confidence level can be defined as

$$P(\Delta\vec{x}) = \int P_2(\vec{x})P_1(\vec{x}+\Delta\vec{x})d^n\vec{x}, \tag{D5}$$

$$1-\alpha = \frac{\int_{P(\Delta\vec{x})>P(0)} P(\Delta\vec{x})d^n\Delta\vec{x}}{\int P(\Delta\vec{x})d^n\Delta\vec{x}}, \tag{D6}$$

where $1-\alpha$ quantifies the degree of incompatibility between knowledge and experiment. In the special case where P_2 is a delta function centered at $\vec{x}_0$, the overlap reduces to

$$P(\Delta\vec{x}) = \int \delta(\vec{x}-\vec{x}_0)P_2(\vec{x}+\Delta\vec{x})d^n\vec{x} = P_2(\vec{x}_0+\Delta\vec{x}). \tag{D7}$$

Then, $\alpha(\vec{x}_0)$ reduces to the significance level defined as the tail probability of highest posterior density region of $P_2(\vec{x}) < P_2(\vec{x}_0)$ as disscussed in the previous example with Gaussian distribution. Note that this analysis applies to probability distributions P_1 and P_2 that are localized and exhibit vanishing tails. The numerical implementation can be found in the GitHub [17].

TABLE VII. Confidence levels $(1-\alpha)$ quantifying the compatibility between posteriors of ΔF for ^{48}Ca and ^{208}Pb based on Skyrme and RMF models and the PREX-2/CREX measurements. Higher values correspond to increased statistical tension between model and experiment.

Posterior	RMF	Skyrme
Basic nuclei	97.0%	99.7%
+PREX	97.4%	99.3%
+CREX	75.8%	97.6%
+PREX + CREX	69.7%	93.5%

Table VII presents the resulting confidence levels $1-\alpha$ quantifying the agreement between theoretical predictions of ΔF from Skyrme and RMF models and the PREX-2/CREX measurements. The theoretical predictions are taken from the posterior distributions discussed in the previous Appendix.

Overall, we observe greater tension between Skyrme predictions and experimental data compared to RMF predictions. This discrepancy primarily arises from the inclusion of the scalar-isovector δ meson in RMF models, with its large Yukawa coupling ($g_\delta^2 \in [0, 1500]$) enhancing the isovector spin-orbit interaction. This leads to an effective spin-orbit parameter $b'_4 \sim 1$ fm^4, whereas the prior used in Skyrme modeling, $b'_4 \in [-0.36, 0.72]$ fm^4, though broader than typical ranges, remains insufficient to reproduce the central values of PREX-2/CREX.

Furthermore, the overlaps between knowledge and experiment are notably higher when only PREX is included, and lower when CREX or both measurements are considered. This indicates that the PREX-2 data are broadly consistent with current theoretical priors and impose minimal update on the posterior, while the CREX measurement is in strong tension with prior expectations.

APPENDIX E: LINEAR CORRELATION BETWEEN S_V, L, b'_4, ΔF^{Ca48}, AND ΔF^{Pb208}

Based on all the samples used in the Bayesian analysis, we found that any three of the variables S_V, L, ΔF^{Ca48}, and ΔF^{Pb208} can form semilinear relations with each other, resulting in four relations as shown in Eqs. (5) and (6). These pocket formulas could help interpret future parity-violating asymmetry experiments. In this Appendix, we explicitly show how these formulas perform for Skyrme and RMF models.

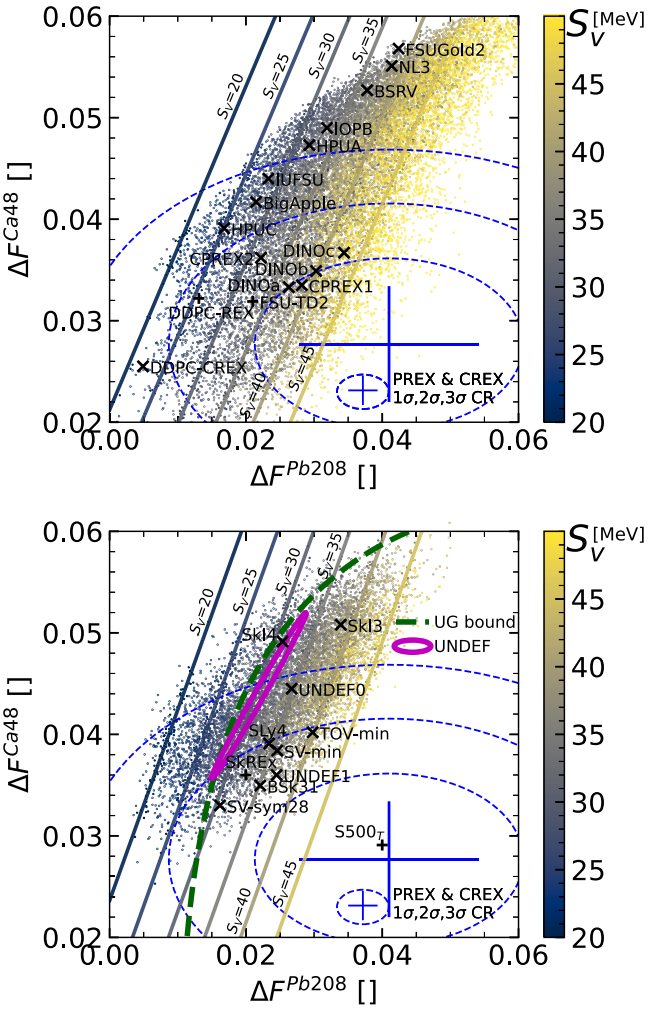


FIG. 8. Similar to Fig. 3 but colored by symmetry energy parameter S_V. Colorful lines correspond to the minimum χ^2 fitting of Eq. (5) with $S_V = [20, 25, 30, 35, 40, 45]$ MeV.

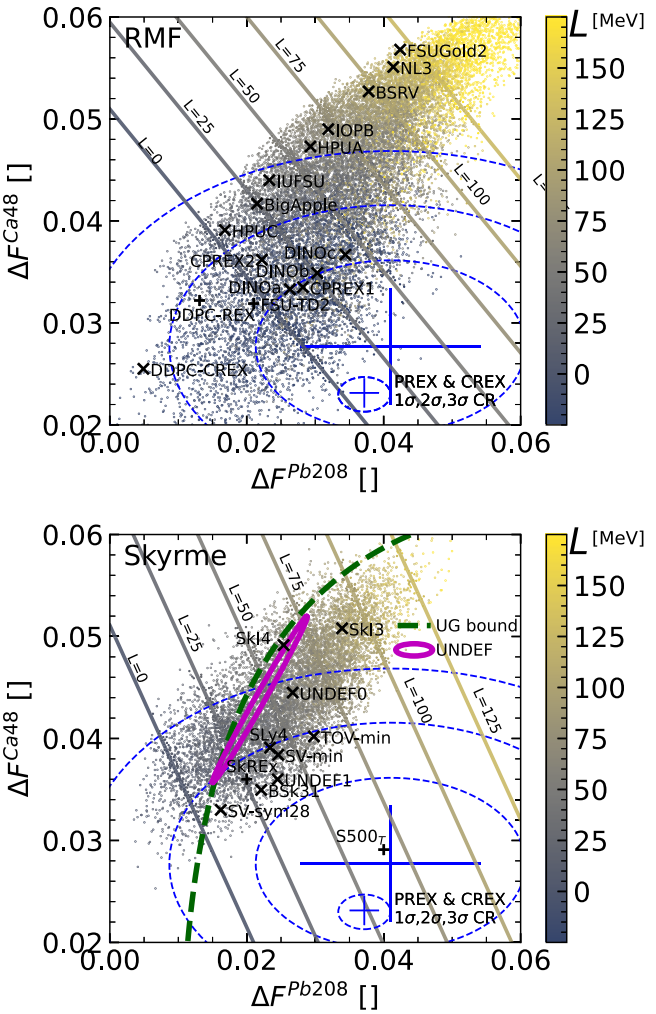


FIG. 9. Similar to Fig. 3 but colored by symmetry energy parameter L. Colorful lines correspond to the minimum χ^2 fitting of Eq. (6) with $L = [0, 25, 50, 75, 100, 125, 150]$ MeV.

Figures 8 and 9 show the distributions of $(\Delta F^{\mathrm{Ca48}}, \Delta F^{\mathrm{Pb208}}, S_{\mathrm{V}})$ and $(\Delta F^{\mathrm{Ca48}}, \Delta F^{\mathrm{Pb208}}, L)$, where the linear correlations in Eqs. (5) and (6) are observed. The precision of the fitting formula in Eq. (5) remains within 10% (1σ) for both Skyrme and RMF models, while Eq. (6) shows about a 10-MeV deviation in the Skyrme model and a 25-MeV deviation in the RMF model. An interesting trend is noted in Fig. 8 for both RMF and Skyrme models: The predicted points of ΔF^{Ca48} and $\Delta F^{\mathrm{Pb208}}$ move *collectively* from left to right (toward the mean of joint PREX-2/CREX measurements) with increasing S_{V}. This collective movement results from S_{V} being sensitive to the neutron skin of ^{208}Pb while being insensitive to the neutron skin of ^{48}Ca in both RMF and Skyrme models. The difference in sensitivity of $\Delta F^{\mathrm{Pb208}}$ and ΔF^{Ca48} to S_{V} is reflected by the slope coefficients a and b in Eq. (5), where b is much larger than a in both Skyrme and RMF fittings.

In Fig. 9, we present the corresponding L values of our sampled points of ΔF^{Ca48} and $\Delta F^{\mathrm{Pb208}}$. As expected, L is sensitive to both the neutron skin of ^{48}Ca and ^{208}Pb, with the points moving collectively from lower left to upper right with increasing L. This movement highlights the challenge of finding parametrizations that satisfy both PREX-2/CREX measurements by only tuning parameters controlling the L values. Notably, for the same L, Skyrme models predict slightly smaller ΔF due to the larger slope of the constant L relation for ΔF compared to RMF models, as seen in Fig. 9. This can be understood from the Pearson correlation coefficient between ΔF and $L(n_B)$ in Fig. 11.

In Fig. 10, we present a more comprehensive demonstration of the b'_4 correlation with ΔF^{Ca48} and $\Delta F^{\mathrm{Pb208}}$ comparing with existing Skyrme and RMF models. The widely used SLy4 model has $W_0 = 2b_4 = 2b'_4 = 123$ MeV fm^5 [43], equivalent to $b_4 = b'_4 = 0.312$ fm^4, which lies on the 2σ contour of the PREX-2/CREX measurement. The first Skyrme models with $b_4 \neq b'_4$, SkI3 and SkI4, are introduced with $b'_4 \leqslant 0 < b_4$, placing them further away from the PREX-2/CREX measurement [38]. SV classes of Skyrme model prefer $0 < b'_4/b_4 < 0.5$; see Fig. 9 in Ref. [46]. TOV-min takes a relatively large $b'_4 = 0.426$ [45], placing it closer toward the right bottom corner. More recent calibrated models UNEDF0 with $b_4 = 0.634$ and $b'_4 = -0.463$ and UNEDF1

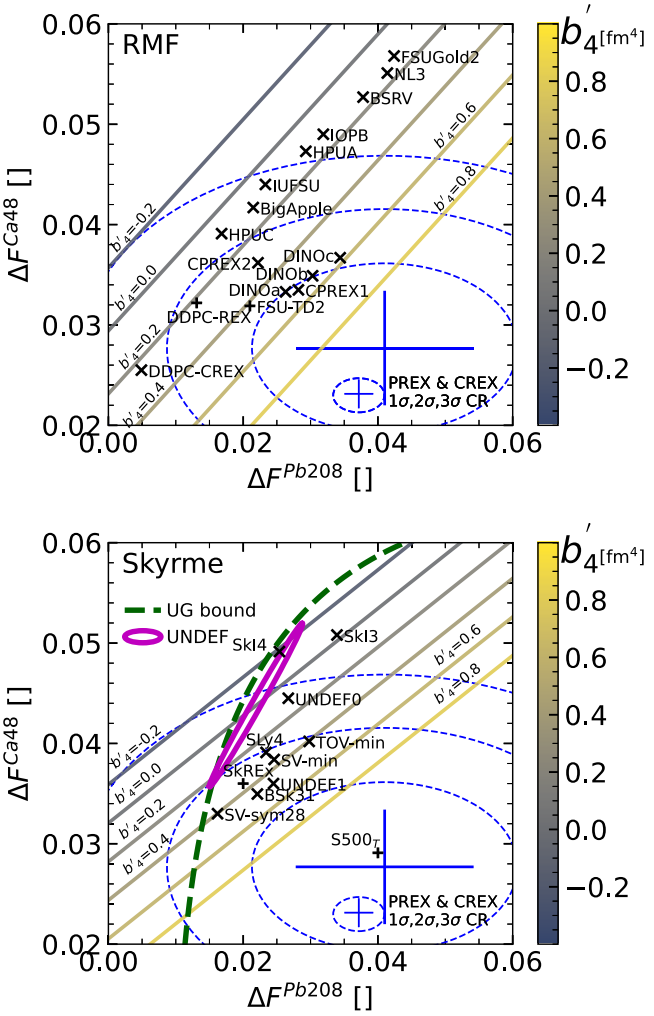


FIG. 10. Similar to Fig. 3 but without colored posterior points for RMF and Skyrme models.

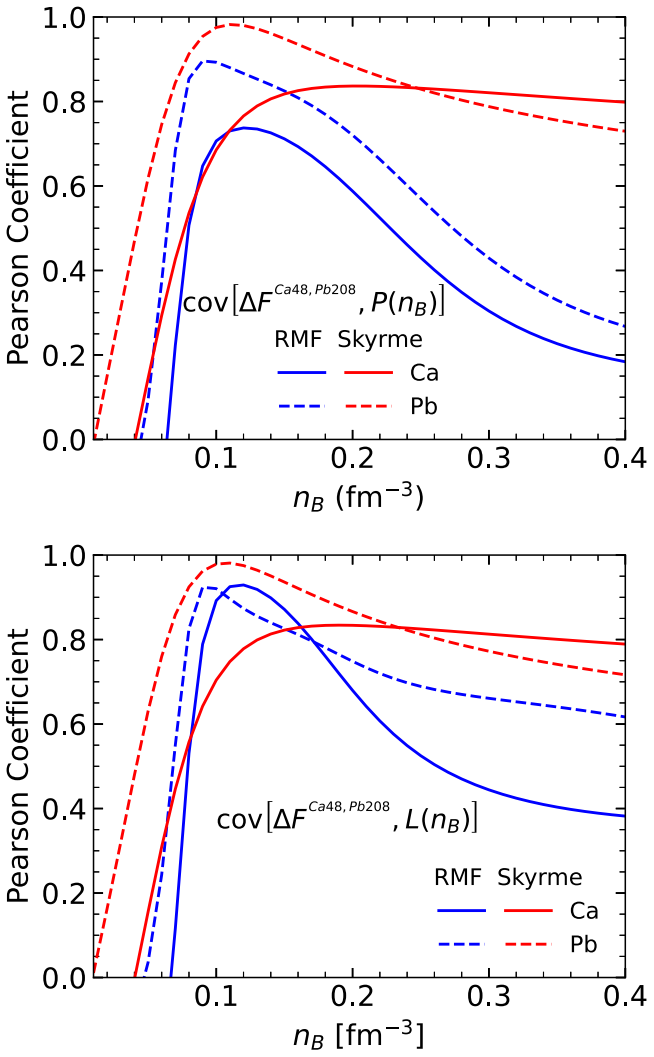


FIG. 11. Pearson correlation coefficient between neutron skin (form factor difference) of ^{48}Ca (solid) and ^{208}Pb (dashed), and pressure (upper panel) or symmetry energy slope (lower panel) at various baryon number densities. Blue and Red correspond to RMF models and Skyrme models.

with $b_4 = 0.194$ and $b'_4 = 0.362$ have b'_4 of opposite sign [47]. Therefore, UNEDF1 is much closer to the PREX-2/CREX measurements compared to UNEDF0. Most recently, the extended Skyrme model with $b'_4 = 1.27$ is proposed to reach the center of PREX-2/CREX measurement [42], which is consistent with our correlation that gives $b'_4 = 1.37 \pm 0.49$ fm^4 for Skyrme models from PREX-2/CREX measurements of ΔF. In the case of RMF models, the effective parameter is $b'_4 = 1.02 \pm 0.37$, corresponding to a 90% lower bound of $b'_4 > 0.544$ fm^4 or $g_\delta^2 + 1.65 g_\rho^2 > 2433$ after incorporating the masses of nucleons and mesons. Widely used RMF models without δ mesons, such as FSUGold2 [49] with $g_\rho^2 = 80.4656$ and FSUGarnet [87] with $g_\rho^2 = 192.9274$, typically exhibit a small effective $b'_4 < 0.1$. Other RMF models with $b'_4 \lesssim 0.1$, such as NL3 [1], IOPB-I [56], IUFSU [50], BigApple [66], and HPUA–C [51], all lie beyond the 2σ region, although these models span a wide range of symmetry energy slope L. RMF models featuring δ mesons with small isovector Yukawa coupling, such as BSRV with $g_\delta^2 < 20$ and $g_\rho^2 < 265$, corresponding to $b'_4 \lesssim 0.1$, also do not show significant improvement [52]. However, models like DINOa–c, which display large isovector Yukawa couplings ($g_\delta^2 > 1100$ and $g_\rho^2 > 800$), all surpass the 90% lower bound of $b'_4 > 0.544$ [10]. Consequently, DINOa–c lies close to the 1σ confidence region of PREX-2/CREX.

In Fig. 11, the Pearson correlation peaks around two-thirds of the saturation density for ^{208}Pb, where the neutron skin correlates well with the form factor difference ΔF for ^{208}Pb. The neutron skin is known to correlate best with the symmetry energy slope at two-thirds of the saturation density for the Skyrme model [88], a correlation confirmed by RMF models as well [89]. Note that for both Skyrme and RMF models, the Pearson correlation between P and $\Delta F^{\mathrm{Pb208}}$ is higher than that between P and $\Delta F^{\mathrm{Ca208}}$ below and around the saturation density. It clearly shows the neutron skin of ^{208}Pb is more sensitive to the pressures in neutron stars than ^{208}Ca does. Additionally, our Pearson correlation study for ΔF^{Ca48} suggests that ΔF^{Ca48} measured in CREX is most sensitive to the symmetry energy slope L at $n_B = 0.12$ fm^{-3} for the RMF model and $n_B = 0.16$ fm^{-3} for the Skyrme model, around saturation density. The Pearson correlations with L are about

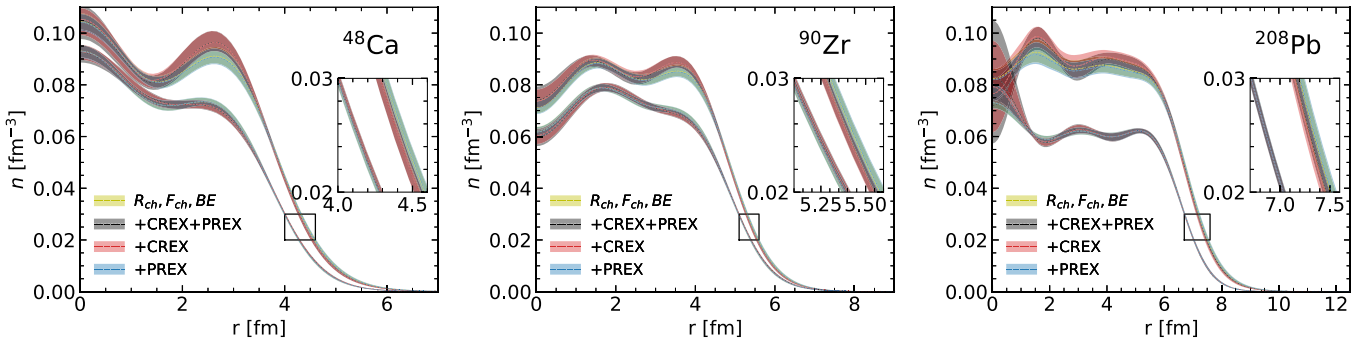


FIG. 12. Vector densities of protons (lower) and neutrons (upper) in ^{48}Ca, ^{90}Zr, and ^{208}Pb. The different colored bands and central lines represent the 18%, 50%, and 82% percentiles under various constraints specified in the legend.

the same between the two nuclei in the RMF models, while the Pearson correlation with L and for ^{208}Pb is much higher than that for ^{48}Ca in Skyrme models, explaining the larger slope of the constant L relation for ΔF.

APPENDIX F: NUCLEON DENSITY DISTRIBUTION OF ^{48}Ca AND ^{208}Pb IN RMF MODEL

In this Appendix, we delve into the proton and neutron density distributions of ^{48}Ca and ^{208}Pb within RMF models, utilizing samples with four different likelihoods. We computed the baryon number density, denoted as $n(r)$, as a function of radius r, and assessed the 18%, 50%, and 82% percentiles of $n(r)$ across all radii.

Figure 12 illustrates the 18%, 50%, and 82% percentiles of proton and neutron densities in ^{48}Ca and ^{208}Pb under various likelihood scenarios. The yellow band represents the basic nuclear constraints outlined in Table VI. Interestingly, this band significantly overlaps with the blue band, which incorporates additional constraints from PREX. This overlap is expected due to the abundance of RMF models in our prior with large S_V and L, coupled with the relatively larger statistical error of PREX compared to CREX. Similar overlaps are observed between the black and red bands. However, the imposition of CREX constraints notably alters the proton and neutron distributions, as evidenced by the discernible differences between the yellow and red bands (or black and blue bands). In ^{48}Ca, the neutron bulge around 2.5 fm increases by approximately 0.005 fm^{-3} with the imposition of CREX constraints, while the distributions for $r < 1$ fm remain unchanged. Consequently, the neutron distribution around the surface contracts inward by about 0.05 fm, resulting in smaller values for $\Delta R_{\rm np}$ and ΔF. Conversely, in ^{208}Pb, the imposition of CREX constraints enhances neutron bulges at 1.5 and 4 fm, while also increasing neutron deficits and proton bulges at the center. Since the central region contributes minimally to the neutron skin, the overall neutron distribution shifts inward, albeit not as significantly as in ^{48}Ca.

As highlighted in our work, the degeneracy (correlation) between $\Delta R_{\rm np}$ (or ΔF) of ^{48}Ca and ^{208}Pb may be mitigated by breaking S_V-L relations or adjusting b'_4. We categorized the sample into five bins based on b'_4 and assessed the 18%, 50%, and 82% percentiles of $n(r)$ accordingly. Figure 13 elucidates how varying b'_4 modulates the density distribution of protons and neutrons. For ^{48}Ca, increasing b'_4 enhances the binding of $1f_{7/2}$ neutron orbit, which amplifies the neutron bulge. At the same time, it weakens $1d_{3/2}$ proton orbit, which suppresses the proton bulge around 2.5 fm. Given that the bulge around 2.5 fm exerts the greatest influence on the overall nucleon distribution due to the r^2 factor in the volume weighting, the heightened isovector density in the bulge precipitates a notable decrease in $\Delta R_{\rm np}$ and ΔF for ^{48}Ca. The behavior of the intermediate nucleus ^{90}Zr appears to mirror that of ^{48}Ca, albeit with slightly smaller variations in magnitude. However, for ^{208}Pb, the radii of both protons and neutrons increase with b'_4. This arises from the reduced binding of the outermost orbitals, namely, $2f_{5/2}$ and $3p_{1/2}$ for neutrons and $1h_{11/2}$ and $2d_{3/2}$ for protons. The $3s$ proton orbit is not sensitive to the spin-orbit interaction and therefore does not contribute appreciably to this trend. As shown in Fig. 13, increasing b'_4 deepens the neutron deficit and enhances the proton bulge at the center, while also diminishing the isovector density at 3 fm. Although neutron excesses increase around 1.5 and 4 fm, the overall neutron excess remains relatively unchanged. Notably, $\Delta R_{\rm np}$ and ΔF exhibit insensitivity or slight positive correlation with b'_4. This can also be seen from Pearson correlation of ΔF in Figs. 5 and 6.

Across all nuclei, a larger b'_4 accentuates the isovector density oscillations throughout the nuclei. However, in ^{48}Ca, these oscillations manifest as a neutron excess in the bulk interior, while maintaining a relatively consistent average neutron excess in the interior of ^{208}Pb. Since a substantial neutron excess in the nuclear interior correlates with a smaller neutron skin and a diminished form factor difference, adjusting b'_4 may break the correlation between $\Delta R_{\rm np}$ (or ΔF) of ^{48}Ca and ^{208}Pb.

In summary, the CREX experiment necessitates a small $\Delta R_{\rm np}$ and ΔF for ^{48}Ca, while the PREX experiment demands a large $\Delta R_{\rm np}$ and ΔF for ^{208}Pb. Given the larger error bars in ΔF for the PREX experiment (three times standard deviation) compared to the CREX experiment, the joint PREX-2/CREX results are predominantly influenced by the CREX experiment, thereby shifting $\Delta R_{\rm np}$ and ΔF for both ^{48}Ca and ^{208}Pb toward smaller values, consistent with other Bayesian analyses [18,19]. If future experiments, such as MREX, confirm the large $\Delta F^{\rm Pb208}$ by narrowing down the statistical error, one potential solution involves introducing a significant isospin-dependent term of the spin-orbit

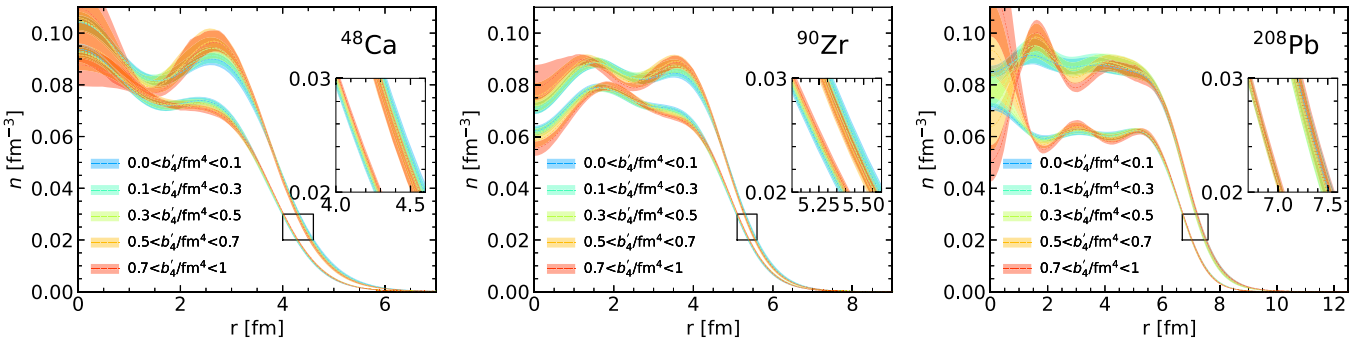


FIG. 13. Similar to Fig. 12. The different colored bands and central lines represent RMF models with various b'_4 defined in Eq. (B17).

interaction to amplify the variation of isovector density. Such variation impacts the average interior neutron excess differently between ^{48}Ca and ^{208}Pb. In this study, we achieve this by adjusting b'_4, although other interactions such as the isovector tensor interaction, may serve a similar purpose [26,42]. Accounting for multiple interactions that excite isovector density oscillations may offer insights into resolving the tension between PREX-2/CREX.

[1] G. A. Lalazissis, J. Konig, and P. Ring, A new parametrization for the Lagrangian density of relativistic mean field theory, Phys. Rev. C **55**, 540 (1997).

[2] K. König *et al.*, Surprising charge-radius kink in the Sc isotopes at N= 20, Phys. Rev. Lett. **131**, 102501 (2023).

[3] F. Sommer *et al.*, Charge radii of ^{55,56}Ni reveal a surprisingly similar behavior at $N = 28$ in Ca and Ni isotopes, Phys. Rev. Lett. **129**, 132501 (2022).

[4] S. Malbrunot-Ettenauer *et al.*, Nuclear charge radii of the nickel isotopes $^{58-68,70}$Ni, Phys. Rev. Lett. **128**, 022502 (2022).

[5] P.-G. Reinhard and W. Nazarewicz, Information content of the differences in the charge radii of mirror nuclei, Phys. Rev. C **105**, L021301 (2022).

[6] W. Koepf and P. Ring, The spin-orbit field in superdeformed nuclei: A relativistic investigation, Z. Phys. A: Hadrons Nucl. **339**, 81 (1991).

[7] C. J. Horowitz and J. Piekarewicz, Neutron star structure and the neutron radius of ^{208}Pb, Phys. Rev. Lett. **86**, 5647 (2001).

[8] D. Adhikari *et al.* (PREX Collaboration), Accurate determination of the neutron skin thickness of ^{208}Pb through parity-violation in electron scattering, Phys. Rev. Lett. **126**, 172502 (2021).

[9] D. Adhikari *et al.* (CREX Collaboration), Precision determination of the neutral weak form factor of ^{48}Ca, Phys. Rev. Lett. **129**, 042501 (2022).

[10] B. T. Reed, F. J. Fattoyev, C. J. Horowitz, and J. Piekarewicz, Density dependence of the symmetry energy in the post-prex-crex era, Phys. Rev. C **109**, 035803 (2024).

[11] B. T. Reed, F. J. Fattoyev, C. J. Horowitz, and J. Piekarewicz, Implications of PREX-2 on the equation of state of neutron-rich matter, Phys. Rev. Lett. **126**, 172503 (2021).

[12] P.-G. Reinhard, X. Roca-Maza, and W. Nazarewicz, Combined theoretical analysis of the parity-violating asymmetry for ^{48}Ca and ^{208}Pb, Phys. Rev. Lett. **129**, 232501 (2022).

[13] G. Hagen *et al.*, Neutron and weak-charge distributions of the ^{48}Ca nucleus, Nat. Phys. **12**, 186 (2016).

[14] B. Hu, W. Jiang, T. Miyagi, Z. Sun, A. Ekström, C. Forssén, G. Hagen, J. D. Holt, T. Papenbrock, S. R. Stroberg, and I. Vernon, *Ab initio* predictions link the neutron skin of ^{208}Pb to nuclear forces, Nat. Phys. **18**, 1196 (2022).

[15] M. H. Mahzoon, M. C. Atkinson, R. J. Charity, and W. H. Dickhoff, Neutron skin thickness of ^{48}Ca from a nonlocal dispersive optical-model analysis, Phys. Rev. Lett. **119**, 222503 (2017).

[16] M. C. Atkinson, M. H. Mahzoon, M. H. Keim, B. A. Bordelon, C. D. Pruitt, R. J. Charity, and W. Dickhoff, Dispersive optical model analysis of ^{208}Pb generating a neutron-skin prediction beyond the mean field, Phys. Rev. C **101**, 044303 (2020).

[17] T. Zhao, GitHub repository: CPREX, https://github.com/sotzee/CPREX.

[18] Z. Zhang and L.-W. Chen, Bayesian inference of the symmetry energy and the neutron skin in ^{48}Ca and ^{208}Pb from CREX and PREX-2, Phys. Rev. C **108**, 024317 (2023).

[19] M. Salinas and J. Piekarewicz, Bayesian refinement of covariant energy density functionals, Phys. Rev. C **107**, 045802 (2023).

[20] S. Gandolfi, J. Carlson, S. Reddy, A. Steiner, and R. Wiringa, The equation of state of neutron matter, symmetry energy and neutron star structure, Eur. Phys. J. A **50**, 10 (2014).

[21] C.-H. Lee, T. T. S. Kuo, G. Li, and G. Brown, Nuclear symmetry energy, Phys. Rev. C **57**, 3488 (1998).

[22] W. Zuo, I. Bombaci, and U. Lombardo, Asymmetric nuclear matter from an extended Brueckner-Hartree-Fock approach, Phys. Rev. C **60**, 024605 (1999).

[23] A. W. Steiner, High-density symmetry energy and direct urca process, Phys. Rev. C **74**, 045808 (2006).

[24] C. Drischler, V. Soma, and A. Schwenk, Microscopic calculations and energy expansions for neutron-rich matter, Phys. Rev. C **89**, 025806 (2014).

[25] B.-J. Cai and L.-W. Chen, Relativistic self-energy decomposition of nuclear symmetry energy and equation of state of neutron matter within QCD sum rules, Phys. Rev. C **100**, 024303 (2019).

[26] M. Salinas and J. Piekarewicz, Impact of tensor couplings with scalar mixing on covariant energy density functionals, Phys. Rev. C **109**, 045807 (2024).

[27] A. W. Steiner, M. Prakash, J. M. Lattimer, and P. J. Ellis, Isospin asymmetry in nuclei and neutron stars, Phys. Rep. **411**, 325 (2005).
[28] C. J. Horowitz, S. J. Pollock, P. A. Souder, and R. Michaels, Parity violating measurements of neutron densities, Phys. Rev. C **63**, 025501 (2001).
[29] W. D. Myers and W. J. Swiatecki, Droplet-model theory of the neutron skin, Nucl. Phys. A **336**, 267 (1980).
[30] M. Centelles, X. Roca-Maza, X. Vinas, and M. Warda, Nuclear symmetry energy probed by neutron skin thickness of nuclei, Phys. Rev. Lett. **102**, 122502 (2009).
[31] M. Warda, X. Viñas, X. Roca-Maza, and M. Centelles, Neutron skin thickness in the droplet model with surface width dependence: Indications of softness of the nuclear symmetry energy, Phys. Rev. C **80**, 024316 (2009).
[32] I. Tews, J. M. Lattimer, A. Ohnishi, and E. E. Kolomeitsev, Symmetry parameter constraints from a lower bound on neutron-matter energy, Astrophys. J. **848**, 105 (2017).
[33] J. Piekarewicz, B. K. Agrawal, G. Colò, W. Nazarewicz, N. Paar, P. G. Reinhard, X. Roca-Maza, and D. Vretenar, Electric dipole polarizability and the neutron skin, Phys. Rev. C **85**, 041302(R) (2012).
[34] M. Kortelainen, T. Lesinski, J. Moré, W. Nazarewicz, J. Sarich, N. Schunck, M. V. Stoitsov, and S. Wild, Nuclear energy density optimization, Phys. Rev. C **82**, 024313 (2010).
[35] C. Drischler, P. Giuliani, S. Bezoui, J. Piekarewicz, and F. Viens, A Bayesian mixture model approach to quantifying the empirical nuclear saturation point, Phys. Rev. C **110**, 044320 (2024).
[36] P. G. Reinhard, X. Roca-Maza, and W. Nazarewicz, Information content of the parity-violating asymmetry in ^{208}Pb, Phys. Rev. Lett. **127**, 232501 (2021).
[37] E. Yüksel and N. Paar, Implications of parity-violating electron scattering experiments on ^{48}Ca (CREX) and ^{208}Pb (PREX-II) for nuclear energy density functionals, Phys. Lett. B **836**, 137622 (2023).
[38] P. G. Reinhard and H. Flocard, Nuclear effective forces and isotope shifts, Nucl. Phys. A **584**, 467 (1995).
[39] C. J. Horowitz and J. Piekarewicz, Impact of spin-orbit currents on the electroweak skin of neutron-rich nuclei, Phys. Rev. C **86**, 045503 (2012).
[40] X. Roca-Maza, G. Colò, and H. Sagawa, Nuclear symmetry energy and the breaking of the isospin symmetry: How do they reconcile with each other? Phys. Rev. Lett. **120**, 202501 (2018).
[41] H. Sagawa, T. Naito, X. Roca-Maza, and T. Hatsuda, Qcd-based charge symmetry breaking interaction and the Okamoto-Nolen-Schiffer anomaly, Phys. Rev. C **109**, L011302 (2024).
[42] T.-G. Yue, Z. Zhang, and L.-W. Chen, PREX and CREX: Evidence for strong isovector spin-orbit interaction, arXiv:2406.03844 [nucl-th].
[43] E. Chabanat, P. Bonche, P. Haensel, J. Meyer, and R. Schaeffer, A Skyrme parametrization from subnuclear to neutron star densities Part II. Nuclei far from stablities, Nucl. Phys. A **635**, 231 (1998); **643**, 441(E) (1998).
[44] E. Chabanat, P. Bonche, P. Haensel, J. Meyer, and R. Schaeffer, A Skyrme parametrization from subnuclear to neutron star densities, Nucl. Phys. A **627**, 710 (1997).
[45] J. Erler, C. J. Horowitz, W. Nazarewicz, M. Rafalski, and P.-G. Reinhard, Energy density functional for nuclei and neutron stars, Phys. Rev. C **87**, 044320 (2013).
[46] P. Klüpfel, P.-G. Reinhard, T. Bürvenich, and J. Maruhn, Variations on a theme by Skyrme: A systematic study of adjustments of model parameters, Phys. Rev. C **79**, 034310 (2009).
[47] M. Kortelainen, J. McDonnell, W. Nazarewicz, P.-G. Reinhard, J. Sarich, N. Schunck, M. Stoitsov, and S. Wild, Nuclear energy density optimization: Large deformations, Phys. Rev. C **85**, 024304 (2012).
[48] S. Goriely, N. Chamel, and J. Pearson, Further explorations of Skyrme-Hartree-Fock-Bogoliubov mass formulas. XVI. Inclusion of self-energy effects in pairing, Phys. Rev. C **93**, 034337 (2016).
[49] W.-C. Chen and J. Piekarewicz, Building relativistic mean field models for finite nuclei and neutron stars, Phys. Rev. C **90**, 044305 (2014).
[50] F. J. Fattoyev, C. J. Horowitz, J. Piekarewicz, and G. Shen, Relativistic effective interaction for nuclei, giant resonances, and neutron stars, Phys. Rev. C **82**, 055803 (2010).
[51] A. Sharma, M. Kumar, S. Kumar, V. Thakur, R. Kumar, and S. K. Dhiman, New equations of state for dense nuclear matter properties, Nucl. Phys. A **1040**, 122762 (2023).
[52] M. Kumar, S. Kumar, V. Thakur, R. Kumar, B. Agrawal, and S. K. Dhiman, CREX- and PREX-II-motivated relativistic interactions and their implications for the bulk properties of nuclear matter and neutron stars, Phys. Rev. C **107**, 055801 (2023).
[53] B. P. Abbott, R. Abbott, T. Abbott, F. Acernese, K. Ackley, C. Adams, T. Adams, P. Addesso, R. X. Adhikari, V. B. Adya *et al.*, GW170817: Measurements of neutron star radii and equation of state, Phys. Rev. Lett. **121**, 161101 (2018).
[54] A. Kunjipurayil, M. Salinas, and J. Piekarewicz, Role of the isovector spin-orbit potential in mitigating the CREX-PREX dilemma, Phys. Rev. C **112**, 014310 (2025).
[55] D. Becker, R. Bucoveanu, C. Grzesik *et al.*, The P2 experiment, Eur. Phys. J. A **54**, 208 (2018).
[56] B. Kumar, S. K. Patra, and B. K. Agrawal, New relativistic effective interaction for finite nuclei, infinite nuclear matter, and neutron stars, Phys. Rev. C **97**, 045806 (2018).
[57] B. Kumar, S. K. Singh, B. K. Agrawal, and S. K. Patra, New parameterization of the effective field theory motivated relativistic mean field model, Nucl. Phys. A **966**, 197 (2017).
[58] J. Yang and J. Piekarewicz, Covariant density functional theory in nuclear physics and astrophysics, Annu. Rev. Nucl. Part. Sci. **70**, 21 (2020).
[59] J. D. Walecka, A theory of highly condensed matter, Ann. Phys. **83**, 491 (1974).
[60] B. D. Serot and J. D. Walecka, The relativistic nuclear many body problem, Adv. Nucl. Phys. **16**, 1 (1986).
[61] B. D. Serot and J. D. Walecka, Recent progress in quantum hadrodynamics, Int. J. Mod. Phys. E **06**, 515 (1997).
[62] S. K. Singh, S. Biswal, M. Bhuyan, and S. Patra, Effects of δ mesons in relativistic mean field theory, Phys. Rev. C **89**, 044001 (2014).
[63] M. Wang, G. Audi, A. H. Wapstra, F. G. Kondev, M. MacCormick, X. Xu, and B. Pfeiffer, The Ame2012 atomic mass evaluation (II), Chinese Phys. C **36**, 1603 (2012).
[64] I. Angeli and K. P. Marinova, Table of experimental nuclear ground state charge radii: An update, At. Data Nucl. Data Tables **99**, 69 (2013).
[65] J. M. Lattimer, Constraints on nuclear symmetry energy parameters, Particles **6**, 30 (2023).

[66] F. Fattoyev, C. Horowitz, J. Piekarewicz, and B. Reed, GW190814: Impact of a 2.6 solar mass neutron star on the nucleonic equations of state, Phys. Rev. C **102**, 065805 (2020).
[67] J. M. Lattimer and F. D. Swesty, A generalized equation of state for hot, dense matter, Nucl. Phys. A **535**, 331 (1991).
[68] C. Horowitz and B. D. Serot, Self-consistent Hartree description of finite nuclei in a relativistic quantum field theory, Nucl. Phys. A **368**, 503 (1981).
[69] P.-G. Reinhard, The relativistic mean-field description of nuclei and nuclear dynamics, Rep. Prog. Phys. **52**, 439 (1989).
[70] P. Ring, Relativistic mean field theory in finite nuclei, Prog. Part. Nucl. Phys. **37**, 193 (1996).
[71] J.-P. Ebran, A. Mutschler, E. Khan, and D. Vretenar, Spin-orbit interaction in relativistic nuclear structure models, Phys. Rev. C **94**, 024304 (2016).
[72] M. Sharma, G. Lalazissis, J. König, and P. Ring, Isospin dependence of the spin-orbit force and effective nuclear potentials, Phys. Rev. Lett. **74**, 3744 (1995).
[73] G. Lalazissis, D. Vretenar, W. Pöschl, and P. Ring, Reduction of the spin-orbit potential in light drip-line nuclei, Phys. Lett. B **418**, 7 (1998).
[74] J. Pearson, Skyrme Hartree–Fock method and the spin–orbit term of the relativistic mean field, Phys. Lett. B **513**, 319 (2001).
[75] B.-A. Li, B.-J. Cai, L.-W. Chen, and J. Xu, Nucleon effective masses in neutron-rich matter, Prog. Part. Nucl. Phys. **99**, 29 (2018).
[76] J. Xu, Z. Zhang, and B.-A. Li, Bayesian uncertainty quantification for nuclear matter incompressibility, Phys. Rev. C **104**, 054324 (2021).
[77] B. Sun, S. Bhattiprolu, and J. M. Lattimer, Compiled properties of nucleonic matter and nuclear and neutron star models from nonrelativistic and relativistic interactions, Phys. Rev. C **109**, 055801 (2024).
[78] M. Tanabashi, K. Hagiwara, K. Hikasa, K. Nakamura, Y. Sumino, F. Takahashi, J. Tanaka, K. Agashe, G. Aielli, C. Amsler *et al.*, Review of particle physics: Particle data groups, Phys. Rev. D **98**, 030001 (2018).
[79] C. Huang, G. Raaijmakers, A. L. Watts, L. Tolos, and C. Providência, Constraining a relativistic mean field model using neutron star mass–radius measurements I: Nucleonic models, Mon. Not. R. Astron. Soc. **529**, 4650 (2024).
[80] N. van Giai and H. Sagawa, Spin-isospin and pairing properties of modified Skyrme interactions, Phys. Lett. B **106**, 379 (1981).
[81] M. Kortelainen, J. McDonnell, W. Nazarewicz, E. Olsen, P.-G. Reinhard, J. Sarich, N. Schunck, S. M. Wild, D. Davesne, J. Erler, and A. Pastore, Nuclear energy density optimization: Shell structure, Phys. Rev. C **89**, 054314 (2014).
[82] P.-G. Reinhard, D. J. Dean, W. Nazarewicz, J. Dobaczewski, J. A. Maruhn, and M. R. Strayer, Shape coexistence and the effective nucleon-nucleon interaction, Phys. Rev. C **60**, 014316 (1999).
[83] P. Danielewicz and J. Lee, Symmetry energy I: Semi-infinite matter, Nucl. Phys. A **818**, 36 (2009).
[84] N. Chamel, S. Goriely, and J. M. Pearson, Further explorations of Skyrme-Hartree-Fock-Bogoliubov mass formulas. IX. Constraint of pairing force to $^1S_0$ neutron-matter gap, Nucl. Phys. A **812**, 72 (2008).
[85] B. K. Agrawal, S. Shlomo, and V. K. Au, Determination of the parameters of a Skyrme type effective interaction using the simulated annealing approach, Phys. Rev. C **72**, 014310 (2005).
[86] J. Friedrich and P.-G. Reinhard, Skyrme-force parametrization: Least-squares fit to nuclear ground-state properties, Phys. Rev. C **33**, 335 (1986).
[87] W.-C. Chen and J. Piekarewicz, Searching for isovector signatures in the neutron-rich oxygen and calcium isotopes, Phys. Lett. B **748**, 284 (2015).
[88] B. A. Brown, Neutron radii in nuclei and the neutron equation of state, Phys. Rev. Lett. **85**, 5296 (2000).
[89] S. Typel and B. A. Brown, Neutron radii and the neutron equation of state in relativistic models, Phys. Rev. C **64**, 027302 (2001).